arXiv:2410.23896v1 [astro-ph.GA] 31 Oct 2024

Exploring the evolution of red and blue galaxies in different cosmic web environments using IllustrisTNG simulation

Biswajit Pandey[a] **and Anindita Nandi**[a]

[a]Department of Physics, Visva-Bharati University, Santiniketan, 731235, India

E-mail: biswap@visva-bharati.ac.in, anindita.nandi96@gmail.com

Abstract. We analyze the evolution of red and blue galaxies in different cosmic web environments from redshift $z = 3$ to $z = 0$ using the IllustrisTNG simulation. We use Otsu's method to classify the red or blue galaxies at each redshift and determine their geometric environments from the eigenvalues of the deformation tensor. Our analysis shows that initially, blue galaxies are more common in clusters followed by filaments, sheets and voids. However, this trend reverses at lower redshifts, with red fractions rising earlier in denser environments. At $z < 1$, most massive galaxies ($\log(\frac{M_*}{M_\odot}) > 10.5$) are quenched across all environments. In contrast, low-mass galaxies ($\log(\frac{M_*}{M_\odot}) < 10.5$) are more influenced by their environment, with clusters hosting the highest red galaxy fractions at low redshifts. We observe a slower mass growth for low-mass galaxies in clusters at $z < 1$. Filaments show relative red fractions (RRF) comparable to clusters at low masses, but host nearly 60% of low-mass blue galaxies, representing a diverse galaxy population. It implies that less intense environmental quenching in filaments allows galaxies to experience a broader range of evolutionary stages. Despite being the densest environment, clusters display the highest relative blue fraction (RBF) for high-mass galaxies, likely due to interactions or mergers that can temporarily rejuvenate star formation in some of them. The $(u - r)$ colour distribution transitions from unimodal to bimodal by redshift $z = 2$ across all environments. At $z < 1$, clusters exhibit the highest median colour, with stellar mass being the primary driver of colour evolution in massive galaxies. The suppression of star formation rate (SFR) and specific SFR (sSFR) is also most pronounced in clusters during this period. Our study suggests that stellar mass governs quenching in high-mass galaxies, while a complex interplay of mass and environment shapes the evolution of low-mass galaxies.

Contents

1 Introduction

Galaxy colour bimodality [1–5] has been recognized for more than two decades. Observations from large galaxy surveys reveal that galaxies cluster into two distinct groups in colour-magnitude diagrams: a red, passive population and a blue, star-forming population. The red galaxies are typically older and have lower star formation rates. Their red colour indicates that they have largely exhausted their supply of gas and are composed of older, cooler stars. In contrast, the blue galaxies are actively forming new stars, which are hotter. These galaxies are generally younger and have a higher rate of star formation.

The implications of colour bimodality for galaxy formation and evolution are significant, as it provides insights into the life cycle of galaxies. Galaxies follow different evolutionary pathways during their evolution. The observed dichotomy suggests that galaxies undergo a transformation from blue to red over time. This transformation may result from external mechanisms such as interactions, mergers, and various environmental effects. Alternatively, internal processes, including gas depletion, stellar evolution, and feedback mechanisms, may also play crucial roles in this transformation. Understanding how different internal processes and external influences shape the observed bimodal colour distribution is essential for gaining a clear picture of galaxy evolution.

Blue galaxies dominate the cosmic landscape at earlier times due to the rising gas fractions at higher redshifts. Star formation in these galaxies is fueled by abundant gas reservoirs. Intense star formation activity depletes the available gas, leading to a decline in the star formation rate with time. As star formation gradually ceases with natural aging, the galaxy eventually becomes red, dominated by older and cooler stars. In addition to natural aging, various internal physical mechanisms, such as morphological quenching [6], mass quenching [7–10], angular momentum quenching [11], and bar quenching [12], can also halt star formation in galaxies. Further, the expulsion or removal of gas from a galaxy provides another effective route for quenching star formation. Gas loss caused by feedback from supernovae, active galactic nuclei, shock-driven winds [14–16] and ram pressure stripping [13] can significantly suppress star formation in galaxies.

Besides the internal processes, environment play a crucial role in transforming blue galaxies into red galaxies. A large body of literature [4, 17–24, 26–29] shows that red and blue galaxies tend to inhabit

high-density and low-density regions, respectively. Various environment-driven mechanisms, such as mergers [30], harassment [31, 32], strangulation [13, 33], starvation [34–36], and satellite quenching [37], can inhibit star formation and alter galaxy structures. Extensive research through simulations [38–52] and observations [53–68] demonstrates that interactions between galaxies, which produce tidal torques, can trigger starbursts and change both the colour and morphology of galaxies.

The environment of a galaxy is often characterized by its local density, but this alone does not describe the neighbourhood of a galaxy. Galaxies are part of a complex cosmic web composed of interconnected filaments, clusters, sheets, and voids [21, 69–77], which collectively organizes and shapes the distribution of matter and galaxies on a grand scale. Studies with N-body simulations reveal a dynamic flow of matter within the cosmic web [78–81], moving from voids to walls, walls to filaments, and finally into clusters.

Filaments are the largest known coherent structures in the universe [82–84]. Hydrodynamical simulations reveal [85, 86] that more than $40\% - 50\%$ of baryonic matter is found in filaments as the Warm-Hot Intergalactic Medium (WHIM). This diffuse medium acts as a gas reservoir that can eventually fall into galaxies, contributing to their growth and affecting their star formation rates. The presence of WHIM can also influence gas accretion efficiency in galaxies. Galaxies in different regions of the cosmic web experience varying levels of gas accretion. For instance, galaxies near the centers of filaments and sheets receive a steady supply of cold gas, which fuels star formation and increases their mass [28, 52, 68, 87–89]. Clusters, the densest regions of the universe, typically form at the intersections of filaments and are characterized by frequent interactions with neighbouring galaxies and extreme environmental conditions, leading to relatively rapid transformations [13, 93, 94]. In contrast, galaxies in lower-density regions like sheets and voids generally follow quieter evolutionary paths with subdued star formation [95, 96]. Thus, different cosmic web environments play a crucial role in shaping the diverse evolutionary trajectories of galaxies across the universe.

Observations reveal that star formation activity in galaxies peaked around a redshift of $z \sim 2 - 3$ [97, 98], an era often dubbed the "cosmic noon". The cosmic star formation rate has seen a dramatic decline from $z = 1$ to $z = 0$ [99]. The number of massive red galaxies with fixed stellar masses has steadily increased since $z \sim 1$ [100, 101]. These trends suggest significant changes in galaxy properties in recent times, which could be crucial in explaining the observed bimodality in galaxy distributions. It is essential to understand how the cosmic web influences the colour bimodality and its evolution.

The IllustrisTNG simulation [102–107] models the formation and evolution of galaxies within the universe. It employs sophisticated numerical techniques to simulate the complex interactions of dark matter, gas, and stars across a vast volume of the universe. It incorporates detailed physics, including gas dynamics, star formation, supernova feedback, and black hole growth, to provide insights into galaxy formation and evolution. This simulation is ideal for studying the roles of different cosmic web environments on galaxy evolution. Several works [102, 108–113] have explored quenching in galaxies using various hydrodynamical simulations. In the present work, we will utilize data from the IllustrisTNG simulation to investigate how different cosmic web environments influence the transformation of galaxy colour since a redshift of $z \sim 3$.

We will categorize the galaxies into red and blue populations based on their colour and stellar mass, following a recently introduced classification scheme [114] based on Otsu's method [115]. We will investigate the evolution of the red and blue fractions in various cosmic web environments. Analyzing these fractions would help us to assess the efficiency of quenching processes within each environment. By tracking how the absolute numbers or percentages of red and blue galaxies change over time, we can understand how quenching impacts galaxy populations in different cosmic web environments. Additionally, we will examine the evolution of the relative red and blue fractions, which reveals how the proportion of red or blue galaxies in a given environment compares to those in all other cosmic environments. This comparison will reveal how the relative abundance of red and blue galaxies in each environment influences the development of colour bimodality. We will also explore how these fractions vary with the stellar mass of galaxies in different cosmic web environments. Studying how the stellar mass dependence of these fractions changes in different environments would help us understand the roles of both environment and stellar mass in shaping the colour bimodality. It is also important to understand how different galaxy properties evolve in different cosmic web environments. To explore

this, we will examine the evolution of median colour, median stellar mass, median star formation rate (SFR), and median specific star formation rate (sSFR) of galaxies with redshift across various cosmic web environments.

The paper is organized into the following sections. In Section 2, we provide a detailed overview of the data used in this work. Section 3 explains the methodology employed for the analysis. The findings are discussed in Section 4, and Section 5 presents the conclusions drawn from our analysis.

2 Data

IllustrisTNG[1] [102–107] is a suite of cosmological gravo-magnetohydrodynamical simulations built on the moving-mesh code AREPO [116, 117]. It serves as an enhanced version of the original Illustris project [118–120]. The TNG suite consists of three cosmological volumes with side lengths of approximately 50, 100, and 300 Mpc, named TNG50, TNG100, and TNG300, respectively. Each volume offers multiple resolution levels, such as TNG100-1, TNG100-2, TNG100-3, and similarly for TNG300, whereas TNG50 has four distinct resolution outputs. All simulations begin at a redshift of $z = 127$, using cosmological parameters from the Planck 2015 results [121]: $\Omega_\Lambda = 0.6911$, $\Omega_m = 0.3089$, $\Omega_b = 0.0486$, $\sigma_8 = 0.8159$, $n_s = 0.9667$, and $h = 0.6774$. For our analysis, we utilize the TNG300-1 run, which offers the largest volume and highest resolution in the TNG series. The specifics of TNG300-1 are detailed in the Table 1, and our study covers redshifts from $z = 3$ to the present ($z = 0$).

Simulation Name	Volume (Mpc^3)	N_{GAS}	N_{DM}	m_{baryon} ($M_\odot$)	m_{DM} ($M_\odot$)
TNG300-1	$(302.6)^3$	2500^3	2500^3	11×10^6	59×10^6

Table 1: This table describes the specifications of the TNG300-1 simulation. Different columns in the table represent the volume of the box (comoving), initial number of gas cells (N_{GAS}), number of dark matter particles (N_{DM}), the target baryon mass (m_{baryon}) and dark matter particle mass (m_{DM}).

At each redshift, we extract various galaxy properties from the publicly available group catalog, which provides details on both halos and subhalos. The FoF algorithm is used to identify halos, while the subhalos (or galaxies) are identified using the SUBFIND algorithm [122, 123]. In this work, we select only galaxies with a non-zero *SubhaloFlag*, as a value of zero indicates a subhalo of non-cosmological origin. Additionally, we impose a stellar mass criterion, choosing galaxies in the range $9 < \log_{10}(\frac{M_\star}{M_\odot}) < 12$. Stellar mass is defined as the total mass of star particles within twice the stellar half-mass radius ($r_{stars}, 1/2$) [105]. For ($u - r$) colour, we use the supplementary catalog provided by [102]. The star formation rates are obtained from the *SubhaloSFRinRad* field in the group catalog. In IllustrisTNG, star formation is modeled following [124]. For our analysis, we use the instantaneous star formation rate, which is the sum of the star formation rates of all star-forming gas cells within twice the stellar half-mass radius of the galaxy.

3 Method

The primary objective of this study is to classify galaxies in the IllustrisTNG simulation into red and blue populations according to their stellar mass and redshift, and to investigate how cosmic web environments and stellar mass influence their evolution.

3.1 Identifying red and blue Galaxies with Otsu's method

Otsu's thresholding technique [115], originally designed for image segmentation, separates data into two groups by minimizing the intra-class variance (variance within each group) and maximizing the inter-class variance (variance between groups). This method iterates through all possible thresholds, selecting the one that provides the optimal separation between the two classes. This technique is particularly useful when the data distribution is bimodal, as is the case with the ($u - r$) colour distribution of
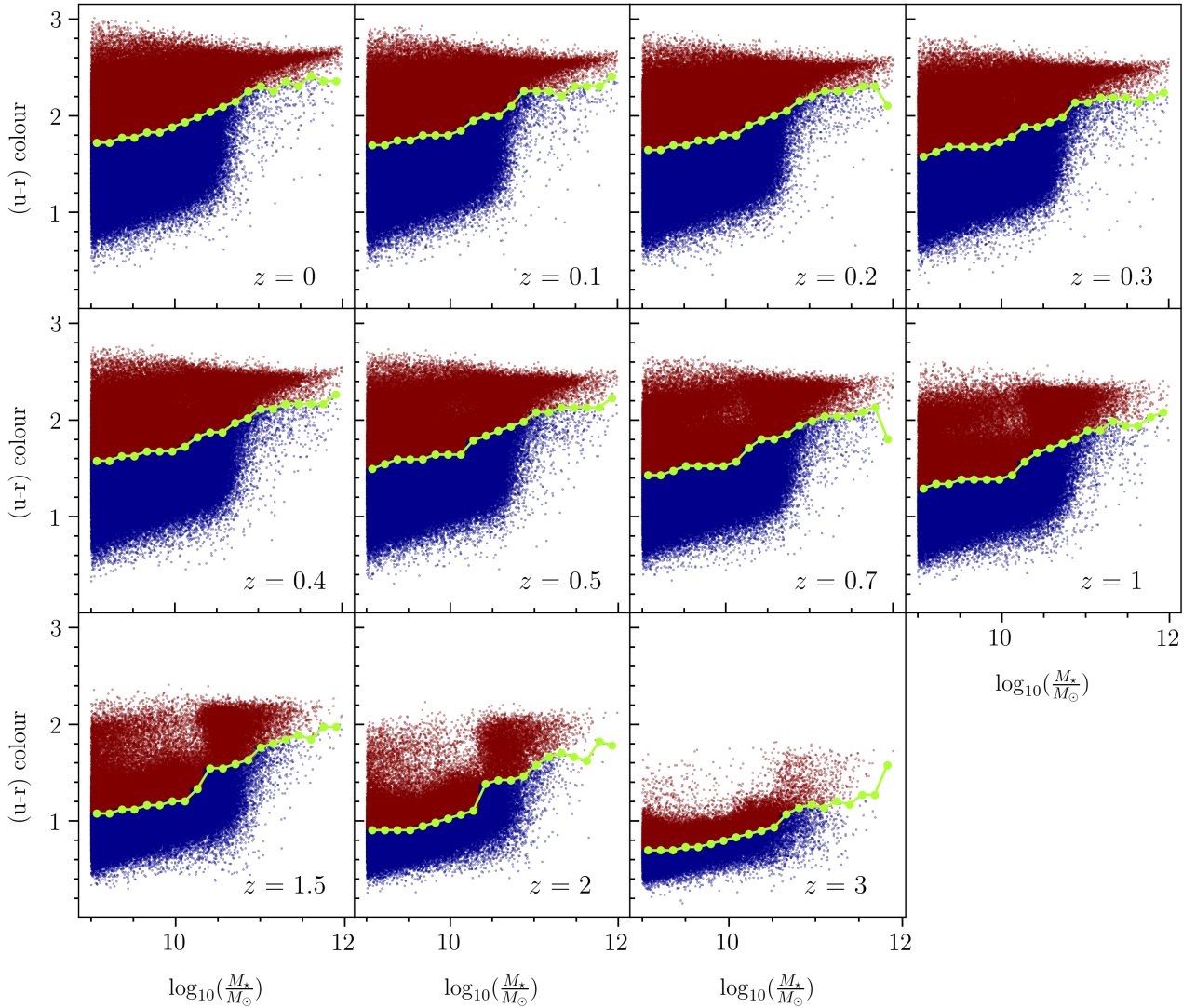
---

[1]

Figure 1: This figure shows the distribution of galaxies in the $(u - r)$ colour-stellar mass plane across each redshift, with the dividing line (determined by Otsu's method) distinguishing the red and blue populations.

galaxies, where we observe two peaks corresponding to the blue cloud and the red sequence. Recently, [114] proposed a method for classifying galaxies into two groups: the "blue cloud" (younger, star-forming galaxies) and the "red sequence" (older, passive galaxies) based on the Otsu's technique.

The primary steps in this method are as follows.

1. Histogram Calculation: We first calculate the histogram of the $(u - r)$ colour for all galaxies in our sample, using a specific number of bins M. The histogram is then normalized by the total number of galaxies $N = \sum_{i=1}^{M} n_i$ where n_i corresponds to the number of galaxies in the ith colour bin. This ensures that the sum of the probabilities for all bins equals to one i.e $\sum_{i=1}^{M} p_i = 1$ where $p_i = \frac{n_i}{N}$.

2. Class Probabilities: For a given threshold, the galaxies are divided into two groups: blue cloud (BC) and red sequence (RS). The probability of each class occurring is calculated based on the proportion of galaxies in each group relative to the total sample. If the threshold is at the k-th bin, the blue cloud is represented by the first k bins, while the red sequence is represented by the bins from $k + 1$ to the end. The class probabilities are given by,

$$P_{BC} = \sum_{i=1}^{k} p_i = w(k) \tag{3.1}$$

and

$$P_{RS} = \sum_{i=k+1}^{M} p_i = 1 - w(k). \tag{3.2}$$

3. Class means and Class variances: We calculate the mean colour and variance for both groups for each threshold value.

The means of the blue cloud and the red sequence are calculated as,

$$\mu_{BC} = \frac{\sum_{i=1}^{k} x_i p_i}{P_{BC}} = \frac{\mu_k}{w(k)} \tag{3.3}$$

and

$$\mu_{RS} = \frac{\sum_{i=k+1}^{M} x_i p_i}{P_{RS}} = \frac{\mu_T - \mu_k}{1 - w(k)} \tag{3.4}$$

Here, x_i represents the $(u - r)$ colour corresponding to the ith bin. The mean up to the kth bin is given by $\mu_k = \sum_{i=1}^{k} x_i p_i$, while $\mu_T = \sum_{i=1}^{M} x_i p_i$ denotes the mean of the entire distribution. It is important to note that $P_{BC} + P_{RS} = 1$ and that $\mu_T = P_{BC} \mu_{BC} + P_{RS} \mu_{RS}$ for every threshold.

Similarly, the class variances are estimated as,

$$\sigma_{BC}^2 = \frac{\sum_{i=1}^{k} (x_i - \mu_{BC})^2 p_i}{P_{BC}} \tag{3.5}$$

and

$$\sigma_{RS}^2 = \frac{\sum_{i=k+1}^{M} (x_i - \mu_{RS})^2 p_i}{P_{RS}} \tag{3.6}$$

4. Intra-class variance and Inter-class variance: The intra-class (within-class) variance (σ_{wc}^2) and the inter-class (between-class) variance (σ_{bc}^2) are calculated as,

$$\sigma_{wc}^2 = P_{BC} \sigma_{BC}^2 + P_{RS} \sigma_{RS}^2 \tag{3.7}$$

and

$$\sigma_{bc}^2 = P_{BC} P_{RS} (\mu_{BC} - \mu_{RS})^2 \tag{3.8}$$

The total variance σ_T^2 is the sum of the two variances,

$$\sigma_T^2 = \sigma_{wc}^2 + \sigma_{bc}^2 \tag{3.9}$$

It is important to note that both σ_{wc}^2 and σ_{bc}^2 are dependent on the selected threshold, while σ_T^2 remains independent of it.

Redshift	Number of galaxies								
	All			$9 < \log_{10}\left(\frac{M_\star}{M_\odot}\right) \leq 10.5$			$10.5 < \log_{10}\left(\frac{M_\star}{M_\odot}\right) < 12$		
	Total	Red	Blue	Total	Red	Blue	Total	Red	Blue
0	253140	130751	122389	225075	105417	119658	28065	25334	2731
0.1	253212	120682	132530	225135	96243	128892	28077	24439	3638
0.2	252546	112362	140184	224612	89094	135518	27934	23268	4666
0.3	251329	105559	145770	223692	83375	140317	27637	22184	5453
0.4	249659	96073	153586	222588	75211	147377	27071	20862	6209
0.5	247760	90513	157247	221341	71415	149926	26419	19098	7321
0.7	242859	81067	161792	218375	64601	153774	24484	16466	8018
1	231933	73719	158214	210682	60488	150194	21251	13231	8020
1.5	199307	69796	129511	184161	61093	123068	15146	8703	6443
2	157394	66878	90516	147377	61740	85637	10017	5138	4879
3	84438	46230	38208	80992	44559	36433	3446	1671	1775

Table 2: This table shows the total number of galaxies with nonzero *SubhaloFlag* and stellar masses within $9 < \log_{10}(\frac{M_\star}{M_\odot}) < 12$ in IllustrisTNG simulation for each snapshot from redshift 0 to 3. It also lists the number of red and blue galaxies identified with the Otsu's method at each redshift in different mass ranges.

5. Threshold Selection: The optimal threshold is the one that minimizes the intra-class variance σ_{wc}^2, which is equivalent to maximizing the inter-class variance σ_{bc}^2. In practice, this threshold can be found by iterating through the possible values and selecting the one that satisfies these conditions. This yields a threshold that is not affected by binning choices, making it a reliable approach for classifying red and blue galaxies [114]. This method offers a robust and parameter-free way to classify galaxies into the blue cloud and red sequence based on their $(u - r)$ colour and stellar mass.

There are distinct relationships between colour and stellar mass or absolute magnitude. Therefore, a single colour threshold cannot be justified for galaxies of varying masses and luminosities. We divide the entire sample into several independent stellar mass bins and apply this technique to each of these bins separately. This provides us a dividing line between the two populations in the colour-stellar mass plane at each redshift (Figure 1). We also tabulate the number of red and blue galaxies in two different mass ranges between redshift 3 to 0 in Table 2.

3.2 Identifying different morphological environments of the cosmic web

We classify galaxies into different morphological environments within the cosmic web using a Hessian-based method [125, 126]. This method relies on the eigenvalues and eigenvectors of the deformation tensor to identify voids, sheets, filaments, and clusters.

The deformation tensor T_{ij} is derived from the Hessian matrix of the gravitational potential field Φ, defined as:

$$T_{ij} = \frac{\partial^2 \Phi}{\partial x_i \partial x_j} \tag{3.10}$$

where x_i and x_j are the spatial coordinates. The gravitational potential Φ is computed by solving the Poisson equation
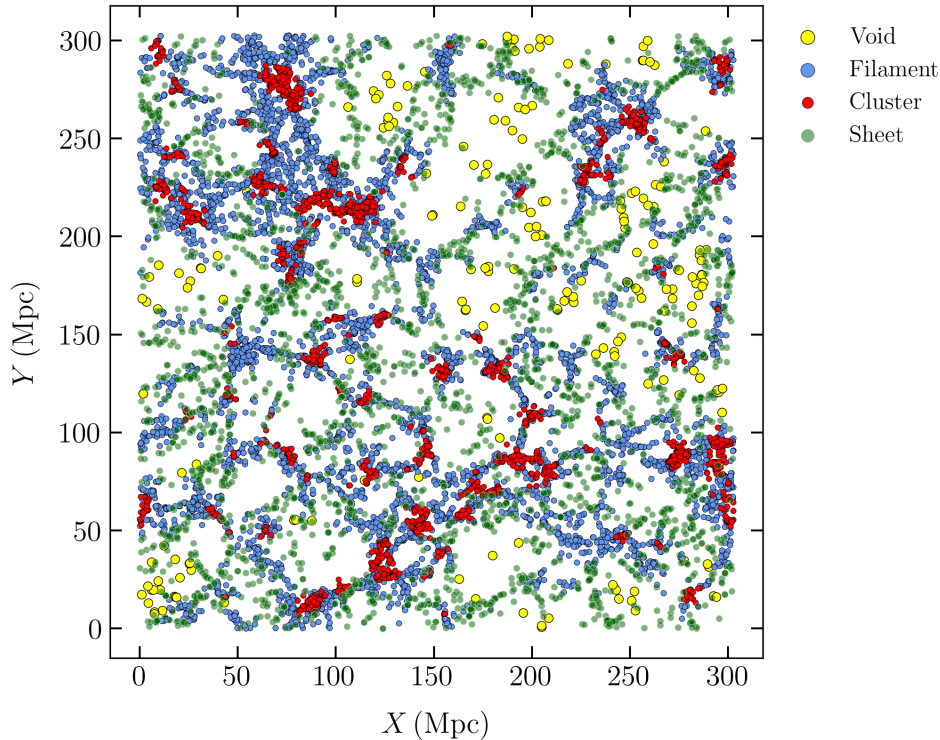
Figure 2: This figure displays the distribution of galaxies in various cosmic web environments at $z = 0$, from a 20 Mpc thick slice of the IllustrisTNG simulation.

$$\nabla^2 \Phi \equiv \delta \tag{3.11}$$

Here, $\delta = \frac{\rho - \bar{\rho}}{\bar{\rho}}$ is the density contrast, with ρ representing the local density and $\bar{\rho}$ the average density. To calculate the potential, we apply the Cloud-In-Cell (CIC) scheme to construct a discrete density contrast field on a grid. This field is smoothed using an isotropic Gaussian filter with a width of 4 Mpc.

Next, we compute the Fourier transform of the gravitational potential:

$$\hat{\Phi} = \hat{G}\hat{\rho} \tag{3.12}$$

where $\hat{G}$ is the Fourier transform of the Green's function of the Laplacian operator, and $\hat{\rho}$ is the density in Fourier space. By transforming the potential back into real space, we calculate the tidal tensor using numerical differentiation.

Based on the signs of the three eigenvalues λ_1, λ_2, and λ_3 (where $\lambda_1 > \lambda_2 > \lambda_3$), galaxies are classified into different cosmic web environments as follows:

1. Void: $\lambda_1, \lambda_2, \lambda_3 < 0$

2. Sheet: $\lambda_1 > 0$, $\lambda_2, \lambda_3 < 0$

3. Filament: $\lambda_1, \lambda_2 > 0$, $\lambda_3 < 0$

4. Cluster: $\lambda_1, \lambda_2, \lambda_3 > 0$

Each type represents a distinct geometric environment in the cosmic web, with voids being underdense and clusters representing the densest regions.

4 Results

4.1 Evolution of red and blue fractions in different cosmic web environments

In this subsection, we examine the evolution of the fraction of red and blue galaxies in various environments within the cosmic web. The red fraction (RF) and blue fraction (BF) in any cosmic web environment are respectively defined as $RF = \frac{n_R}{n_R+n_B}$ and $BF = \frac{n_B}{n_R+n_B}$. Here, n_R and n_B are the number of red and blue galaxies in the same environment. The top left and bottom left panels of Figure 3 illustrate these fractions across different cosmic web environments. Although the blue fraction can be obtained by simply subtracting the red fraction from one, they are separately shown here for the sake of completeness.

At redshift $z = 3$, the blue fraction is highest in clusters, followed by filaments, sheets, and voids. Specifically, the blue fraction is $\sim 48\%$ in clusters and around 40% in voids. Although the differences in blue fraction across environments at $z = 3$ are not substantial, the trend suggests that overdense regions were more conducive to star formation in earlier times. This may arise due to the presence of larger gas reservoirs in these regions.

As redshift decreases, the blue fraction increases in all cosmic web environments. However, this trend reverses at lower redshifts, with the blue fraction declining and the red fraction rising. The blue fraction decreases and the red fraction increases at specific redshifts, with inflection points occurring at $z = 1.5$ for clusters, $z = 0.7$ for filaments and sheets, and $z = 0.5$ for voids. At $z \leq 1.5$, red fractions dominate in clusters, followed by filaments, sheets, and voids. By $z = 0$, the red fraction becomes 75% in clusters, 45% in filaments, 34% in sheets, and 30% in voids.

These results indicate an environment-dependent trend in galaxy colour transformation. Physical mechanisms that suppress star formation are more dominant in clusters and become effective earlier. This may be due to gradual gas depletion from ongoing star formation and faster gas exhaustion from interaction-induced starbursts in high-density regions. Suppression of star formation is less effective in filaments and least effective in sheets and voids, as evidenced by a high blue fraction ($\sim 68\%$) in these environments. This is also supported by a relatively smaller reduction in the blue fraction in sheets and voids from their respective peak values ($\sim 78\%$ at $z = 0.5$).

We now divide our galaxy sample at each redshift into two distinct mass bins: $9 < \log(\frac{M_*}{M_\odot}) \leq 10.5$ and $10.5 < \log(\frac{M_*}{M_\odot}) < 12$ to examine the evolution of red and blue fractions in lower and higher mass galaxies separately. Results for these two mass bins are presented in the middle and right panels of Figure 3. The middle panels display the evolution of red and blue fractions for the lower mass bin, which includes approximately $\sim 90\%$ galaxies of the entire sample (Table 2). The results for the lower mass bin are quite similar to those for the entire sample for this reason.

The results for the higher mass bin, containing about $\sim 10\%$ of the galaxies, are shown in the right panels of Figure 3. Even for the galaxies in the higher mass bin at $z = 3$, we observe a higher blue fraction and a lower red fraction in clusters compared to filaments and sheets. However, the red fraction steadily increases across all environments as redshift decreases, indicating that star formation is gradually suppressed in massive galaxies regardless of their environment. Notably, the blue fraction in voids increases between $z = 2$ and $z = 1$, suggesting that massive galaxies in voids may follow different evolutionary trajectories compared to those in other cosmic web environments.

4.2 Stellar mass dependence of the red and blue fractions in different cosmic web environments and their evolution

We also examine the red and blue fractions as functions of stellar mass within each geometric environment. Figure 4 and Figure 5 show these results across different redshifts. The bottom right panels of these figures reveal that at $z = 3$, clusters generally have a higher blue fraction and a lower red fraction across nearly all masses. The blue fraction in filaments is lower than in clusters but higher than in sheets and voids throughout the entire mass range. However, the larger error bars for voids and sheets limit the statistical significance of these differences. Between $z = 3 - 1.5$, we observe that in each geometric environment, the blue fraction increases significantly in lower mass galaxies ($\log(\frac{M_*}{M_\odot} \leq 10.5)$. The blue fraction in lower mass galaxies do not exhibit a strong dependence on the geometric environment during this period. A clear environment-dependent trend emerges at $z < 1$.
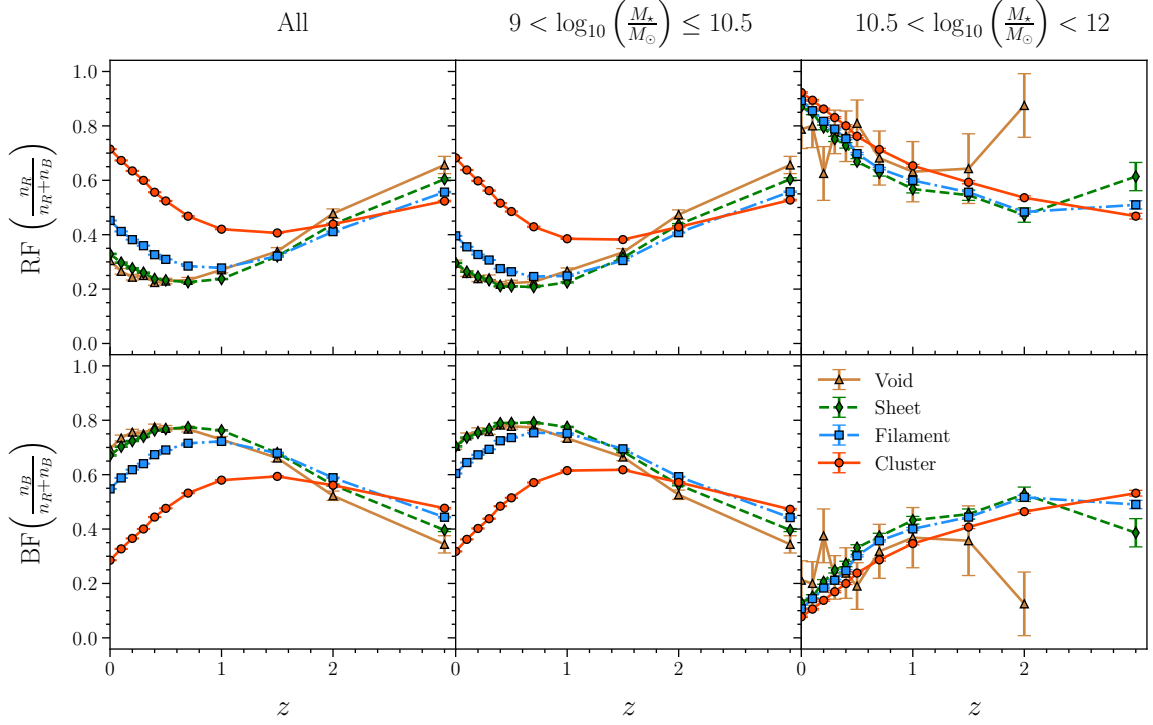
Figure 3: The panels in this figure display the red and blue fractions across various cosmic web environments, plotted as a function of redshift for different mass ranges. The 1σ Binomial errorbars are shown at each data point.
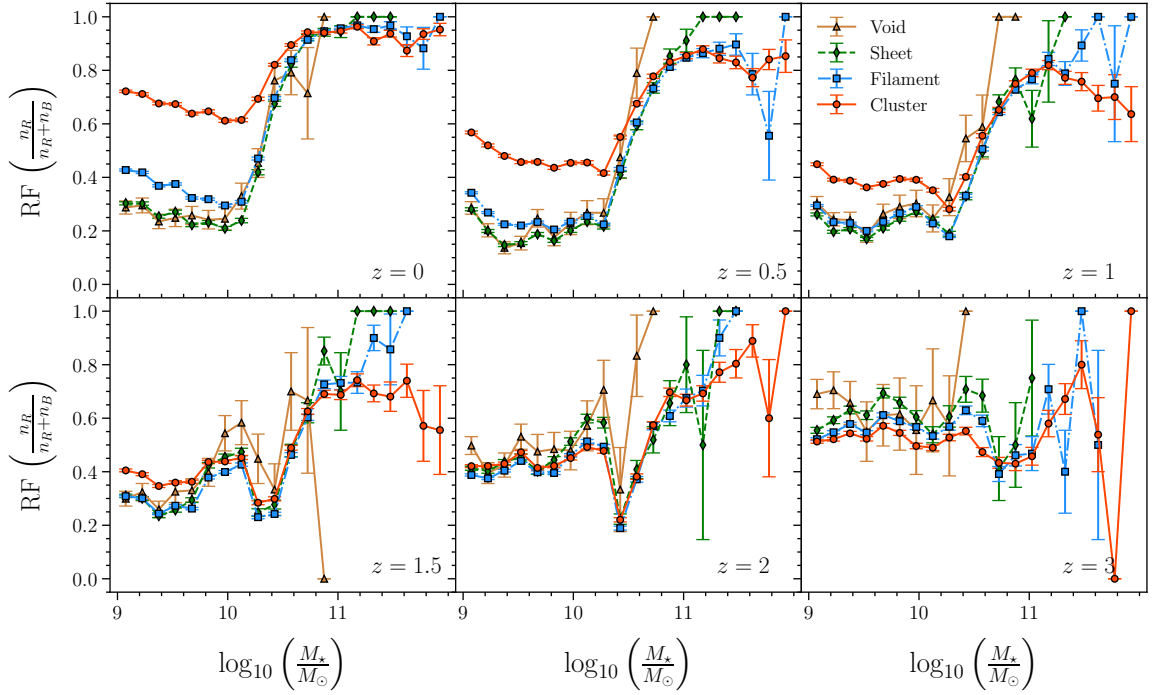

Figure 4: The panels of this figure show the red fraction as a function of stellar mass in different cosmic web environments at different redshifts. The 1σ Binomial errorbars are shown at each data point.
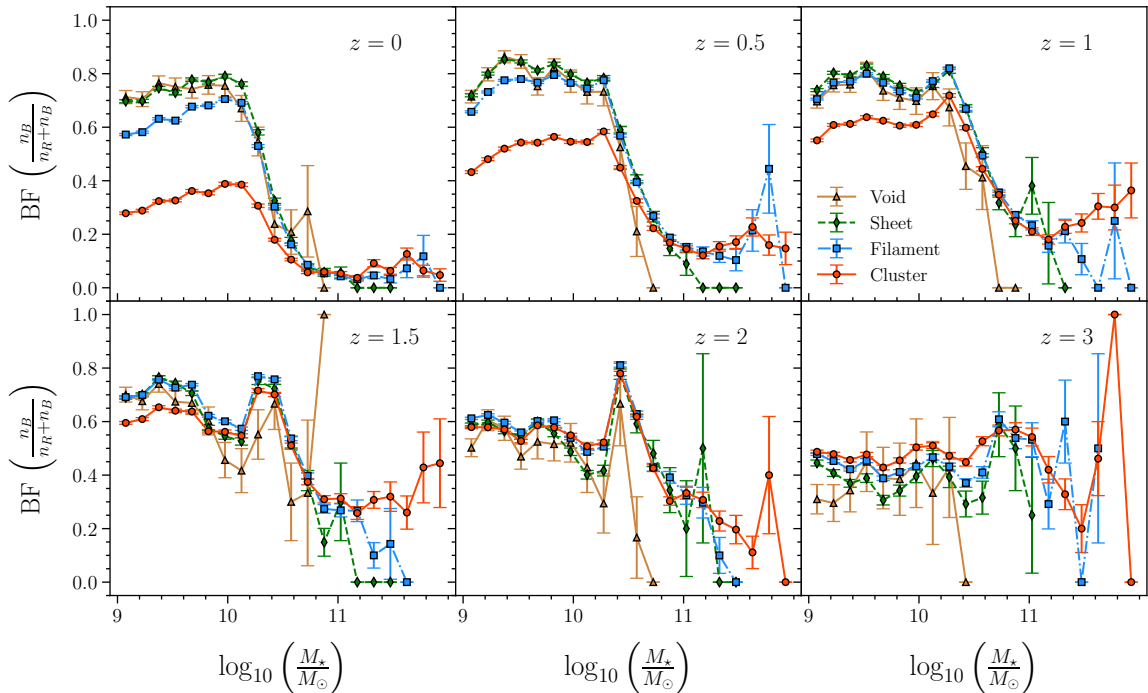
Figure 5: Same as Figure 4 but for blue fraction.

We find that in clusters, the red fraction of lower mass galaxies increases from approximately $\sim 40\%$ to $\sim 70\%$ between redshifts 1 and 0. For higher mass galaxies, the red fraction rises from about $\sim 80\%$ to $\sim 95\%$ in all environments over the same period. Further, $\sim 40\%$ of galaxies in filaments are red, compared to around $\sim 30\%$ in sheets and voids. This indicates that the quenching of lower mass galaxies is strongly influenced by their environment at $z < 1$, while quenching in more massive galaxies is less affected by their embedding geometric environments during the same period.

4.3 Evolution of relative red and blue fractions in different cosmic web environments

The red and blue fractions provide the proportion of two populations in any particular environment. We can use the relative red fraction (RRF) and the relative blue fraction (RBF) to study the relative abundance of red and blue galaxies in various cosmic web environments. The RRF and RBF are respectively defined as $RRF = \frac{(n_R)_i}{\sum_{i=1}^{4} (n_R)_i}$ and $RBF = \frac{(n_B)_i}{\sum_{i=1}^{4} (n_B)_i}$, where $(n_R)_i$ and $(n_B)_i$ are the numbers of red and blue galaxies in i^{th}-type environment. Here i runs from 1 to 4 covering 4-types of cosmic web environment. We examine the evolution of the RRF and RBF across different cosmic web environments, as shown in the top and bottom left panels of Figure 6. The RRF and RBF represent the proportions of red and blue galaxies, respectively, within a specific environment compared to other cosmic environments. The top and bottom left panels of Figure 6 reveal that in filaments and sheets, the RRF decreases and the RBF increases with decreasing redshift. Conversely, clusters show an opposite trend where the RRF increases and the RBF decreases as redshift decreases. Throughout the entire redshift range, filaments consistently have the highest RBF. At lower redshifts ($z < 1$), clusters exhibit the highest RRF compared to other environments.

The middle and right panels of Figure 6 present the RRF and RBF for lower and higher mass bins, respectively. The trends observed in the lower mass bin mirror those of the entire sample, given that most galaxies belong to the lower mass category. In the higher mass bin, the behavior of the RRF and RBF is less intuitive. Specifically, both RRF and RBF decrease in clusters with decreasing redshift, while they increase in filaments and sheets. For higher mass galaxies, clusters have higher RRF and RBF than filaments at earlier times ($z > 1$), but this trend reverses at $z \sim 1$, with filaments surpassing clusters in both RRF and RBF. This counter-intuitive result can be explained by examining the relative proportions of galaxies in different cosmic web environments.

Figure 7 illustrates the evolution of the relative fractions of galaxies in filaments, sheets, clusters,
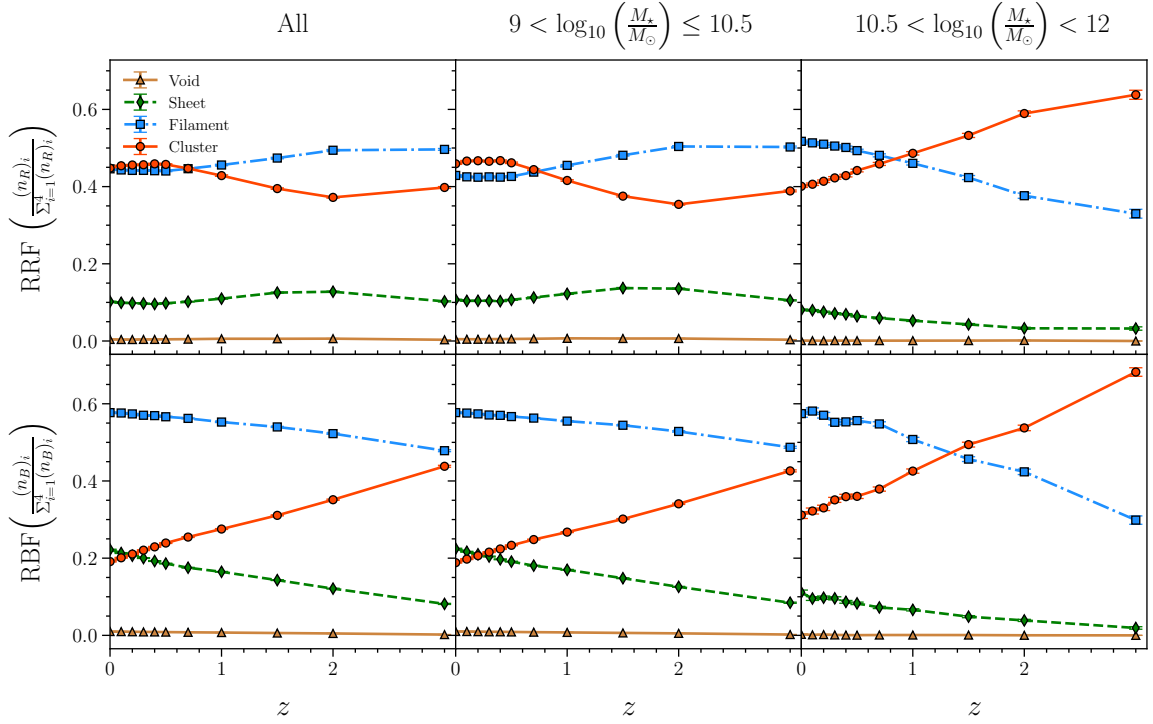
Figure 6: The panels in this figure show the evolution of the relative red fraction (RRF) and relative blue fraction (RBF) in different cosmic web environments with redshift for different mass ranges. The errorbar shown at each data point represents the 1σ Binomial errorbar.
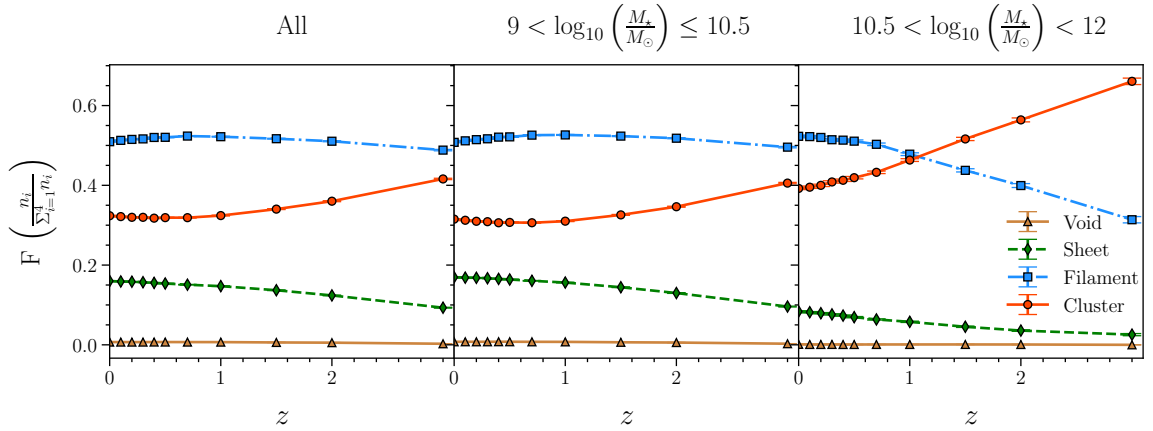

Figure 7: The panels in this figure show the evolution of the relative fraction of galaxies in different cosmic web environments with redshift for different mass ranges. The 1σ Binomial errorbars are shown at each data point.

and voids for the entire sample and the two distinct mass bins. The left panel of Figure 7 shows that filaments generally have the highest galaxy abundance, followed by clusters, sheets, and voids across the entire redshift range. The proportion of galaxies in filaments and sheets increases with decreasing redshift, while the proportion in clusters decreases. These trends are also evident in the lower mass bin, as depicted in the middle panel of Figure 7. In the high mass bin, the proportion of galaxies in filaments and clusters evolves differently, as shown in the right panel of Figure 7. There is a crossover around $z \sim 1$, after which filaments have a higher proportion of galaxies compared to clusters. Prior to $z = 1$, clusters dominate in terms of galaxy proportion.

The anomalous results in the right panels of Figure 6 are explained by the trends observed in the right panel of Figure 7 and Figure 3. For high mass galaxies, RF increases and BF decreases in all types of cosmic web environments, with comparable values across different environments (Figure 3).

Consequently, the magnitudes of the RRF and RBF are primarily determined by the proportions of galaxies in different environments. The trends observed in the right panel of Figure 7 are reflected in the top and bottom right panels of Figure 6, with crossovers in RRF and RBF occurring at different redshifts due to the varying red and blue fractions in filaments and clusters.

It may be noted that the red fraction (RB) and blue fraction (BF) are complementary to each other, meaning that their sum always equals 1. However, this relationship does not extend to the relative red fraction (RRF) and relative blue fraction (RBF). In other words, knowing the RRF does not allow us to directly infer the RBF.

4.4 Stellar mass dependence of the relative red and blue fractions in different cosmic web environments and their evolution

We now examine the RRF and RBF across different cosmic web environments as functions of stellar mass and their evolution from redshift 3 to 0. The various panels in Figure 8 display the RRF as a function of stellar mass in different cosmic web environments at different redshifts. The results indicate that in both filaments and sheets, the RRF is lower at higher masses and higher at lower masses. The RRF in filaments and sheets at lower masses decreases with decreasing redshift. Conversely, clusters exhibit an opposite trend, where the RRF is higher at higher masses and lower at lower masses. In clusters, the RRF at higher masses remains relatively stable with redshift, while at lower masses, it gradually increases as redshift decreases. At $z \sim 1$, the RRF at lower masses becomes comparable between filaments and clusters. However, below this redshift, clusters tend to dominate at lower masses, while filaments become more prominent at intermediate masses. At low redshifts, the RRF in clusters exceeds that of all other environments at both low and high masses. This suggests that low-mass red galaxies in clusters may represent quenched satellites, while high-mass red galaxies may be massive centrals. Interestingly, the RRF in clusters and filaments shows two distinct crossovers at intermediate masses. Between these crossovers ($10.5 < \log(\frac{M_*}{M_\odot}) < 11$), the RRF in filaments surpasses that of all other environments. It may be worthwhile to mention here that the right panels of Figure 6 indicate that, at lower redshifts, both RRF and RBF dominate in filaments for masses $\log(\frac{M_*}{M_\odot}) > 10.5$. However, a closer examination reveals that this dominance is confined to the mass range $10.5 < \log(\frac{M_*}{M_\odot}) < 11$. There are only a small number of red and blue galaxies with masses $\log(\frac{M_*}{M_\odot}) > 11$, and these primarily reside in clusters.

We present the RBF as a function of stellar mass across different cosmic web environments and redshifts in the various panels of Figure 9. Our analysis reveals that in both filaments and sheets, the RBF is lower at higher masses and higher at lower masses. Specifically, the RBF in filaments and sheets at lower masses increases as redshift decreases. Between redshift $z = 1 - 0$, filaments exhibit a significantly higher RBF (~ 0.55) compared to other environments for galaxies having $\log(\frac{M_*}{M_\odot}) < 11$. This indicates that filaments host a diverse population of galaxies, encompassing both passive and star-forming galaxies. The less aggressive environmental quenching in filaments allows for a wider range of evolutionary stages. Interestingly, despite being the densest environment, clusters show the highest RBF for high-mass galaxies ($\log(\frac{M_*}{M_\odot} > 11$) even at lower redshifts. This suggests that clusters are highly dynamic environments where interactions or mergers might temporarily reignite star formation activity in some high mass galaxies.

4.5 Evolution of colour across different cosmic web environments

We present the distributions of $(u - r)$ colour across various cosmic web environments at different redshifts, ranging from $z = 3$ to $z = 0$, as shown in different panels of Figure 10. At $z = 3$, the $(u - r)$ colour distribution in each environment is unimodal, with a peak around $(u - r) \sim 0.7$. As redshift decreases, this peak shifts towards higher $(u-r)$ values, indicating the aging of stellar populations. By $z = 2$, the colour distribution begins to show bimodality. The bimodality becomes most pronounced in clusters, followed by filaments, sheets, and voids. In clusters, the peak corresponding to the red sequence grows rapidly, eventually surpassing the peak of the blue cloud in this environment at $z = 0.5$. The emergence of distinct bimodality across all environments suggests that the colour transformation can occur in any cosmic web environment.
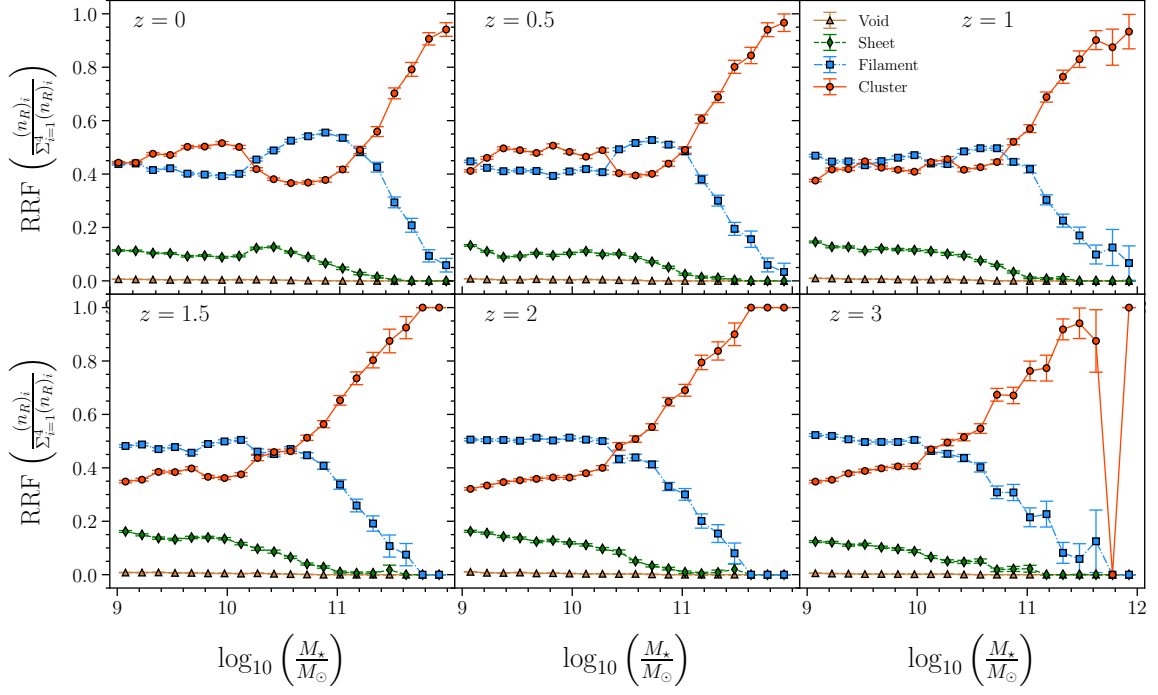
Figure 8: This shows the RRF as a function of stellar mass for different geometric environments at different redshifts between 3 to 0. We show the 1σ Binomial errorbars at each data point.
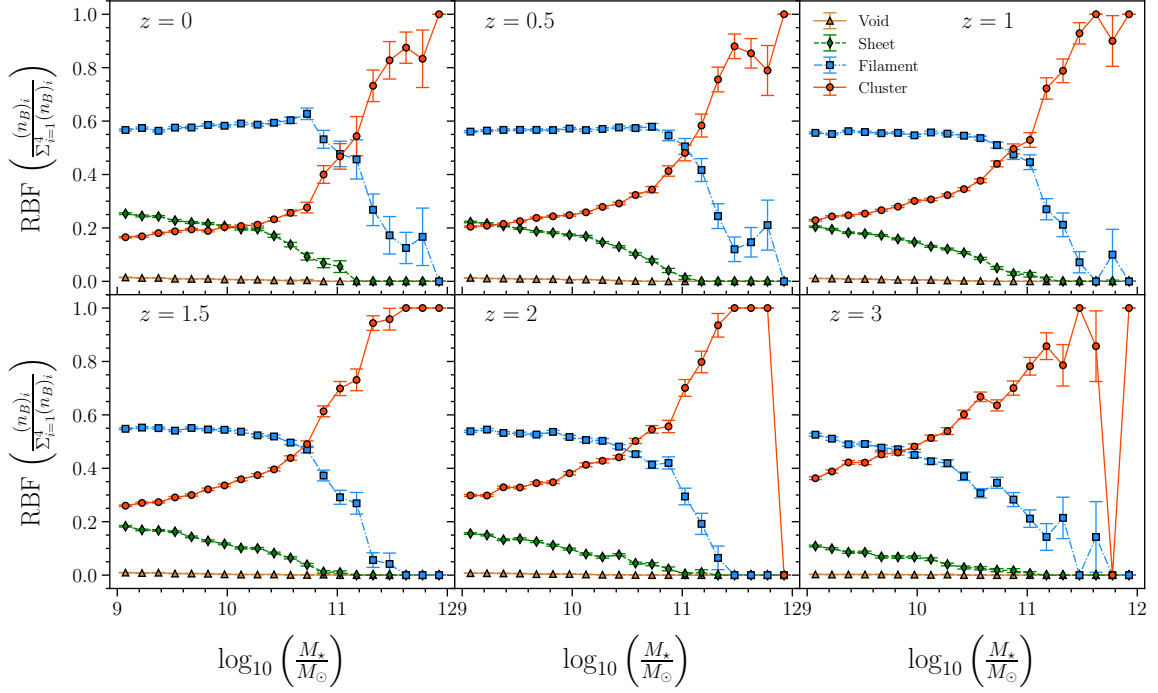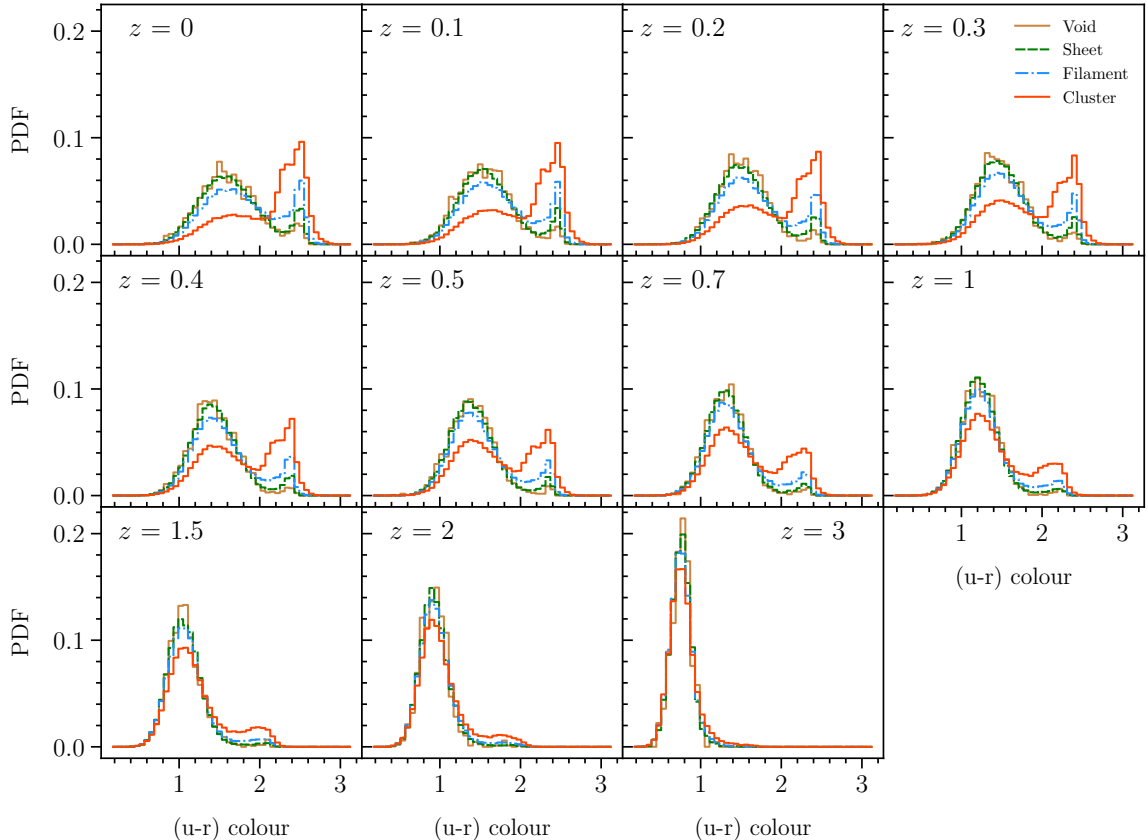

Figure 9: Same as Figure 8 but for RBF.

Figure 10: This figure shows the PDF of $(u-r)$ colour in different cosmic web environments at different redshifts.

In the top left panel of Figure 11, we show the median $(u-r)$ colour of galaxies in various cosmic web environments as a function of redshift. Since $z \sim 2$, the median colour in clusters begins to diverge from that in other environments and increases rapidly after $z > 1$. Meanwhile, the median colour in filaments starts to differ from that in sheets and voids after redshift 1. At $z < 1$, clusters exhibit the highest median colour, followed by filaments, sheets, and voids.

The top right and bottom panels of Figure 11 illustrate the evolution of the median colour in each environment for lower and higher mass bins. The lower mass bin shows trends similar to the combined sample due to the large number of galaxies in this bin. The bottom panel reveals that the median colour for more massive galaxies ($10.5 < \log(\frac{M_*}{M_\odot}) < 12$) increases steadily at $z < 1$, with little variation across different environments. This suggests that the colour evolution of the more massive galaxies is primarily driven by mass and is less dependent on their environment. This reaffirms our findings in subsection 4.1 and subsection 4.2.

4.6 Evolution of stellar mass across diverse cosmic web environments

We present the stellar mass distributions of galaxies across different environments from $z = 3$ to $z = 0$ in Figure 12. At higher masses, galaxies are predominantly found in clusters, followed by filaments, sheets, and voids. Conversely, at lower masses, the distribution is dominated by galaxies in voids, with fewer in sheets, filaments, and clusters. This trend indicates that massive galaxies are more common in clusters and filaments, while less massive galaxies are more prevalent in sheets and voids. At $z < 2$, we observe the emergence of a bump in the stellar mass distribution around $\log(\frac{M_*}{M_\odot} \sim 10.5)$ in each environment. The bump becomes more pronounced in all environments after $z = 1$ suggesting an increase in the number of intermediate-mass galaxies during this period.

In the top left panel of Figure 13, we show the evolution of the median stellar mass of galaxies across different cosmic web environments. It shows that as redshift decreases, the median mass of galaxies increases in all environments. At each redshift, the median mass is highest in clusters, followed
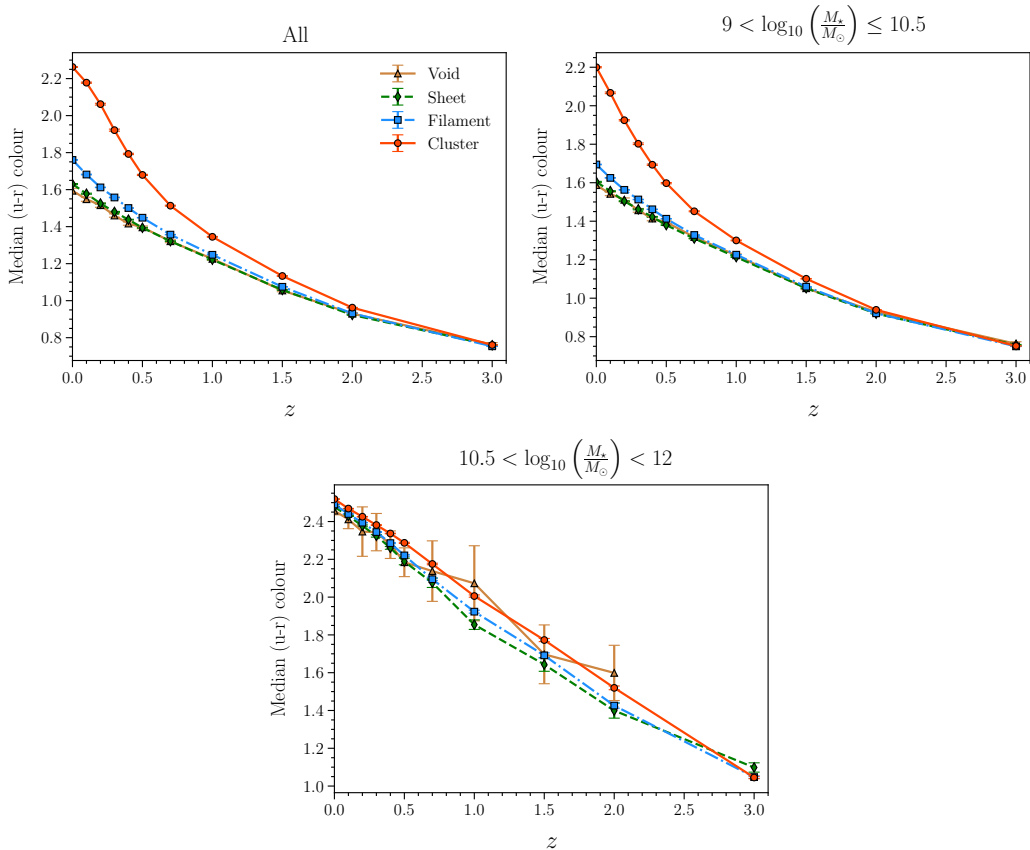
Figure 11: This figure shows the evolution of median $(u-r)$ colour in different cosmic web environments with redshift. The top left panel shows the results for the entire sample. The top right panel and the bottom panel show the results for the lower and higher mass bin respectively. The 1σ errorbars are calculated using 50 bootstrapped realizations from the original data.

by filaments, sheets, and voids. The top right and bottom panels of Figure 13 show the results for lower and higher mass bins, respectively. In the top right panel, we observe that the median mass of galaxies in filaments and sheets increases steadily between $z = 1$ and $z = 0$. However, at $z < 1$, the growth rate of the median mass for lower mass galaxies in clusters slows down significantly compared to those in filaments and sheets. The bottom panel shows that the median stellar mass for high mass galaxies remains stable between $z = 3$ and $z = 1.5$, followed by a gradual increase up to the present. This suggests that these galaxies undergo a period of minimal mass growth during the earlier stages of cosmic evolution, likely indicating that major mergers are less frequent at higher redshifts. The steady increase in median stellar mass at $z < 1.5$ points to more significant mass accumulation in later stages, possibly due to mergers and accretion.

It may be interesting to note that while the median colour of massive galaxies is quite similar across different environments (as shown in Figure 11), their median mass differs significantly.

4.7 Evolution of SFR across diverse cosmic web environments

The SFR distributions of galaxies in various cosmic web environments are shown at different redshifts in the panels of Figure 14. The peak location of the SFR distribution shifts from $\log(SFR) = 0.75$ to $\log(SFR) = -0.5$ over the redshift range $z = 3$ to $z = 0$. While the peak locations differ slightly across cosmic web environments between redshifts $z = 3$ and $z = 1$, they converge to nearly the same $\log(SFR)$ value at $z < 1$. The peak amplitude is highest in voids, followed by sheets, filaments, and clusters.

We show the evolution of the median SFR in different environments in the three panels of Figure 15. The top left panel shows that the median SFR is highest in clusters, followed by filaments, sheets, and voids until $z = 1.5$. The median SFR in clusters becomes smaller than the other geometric
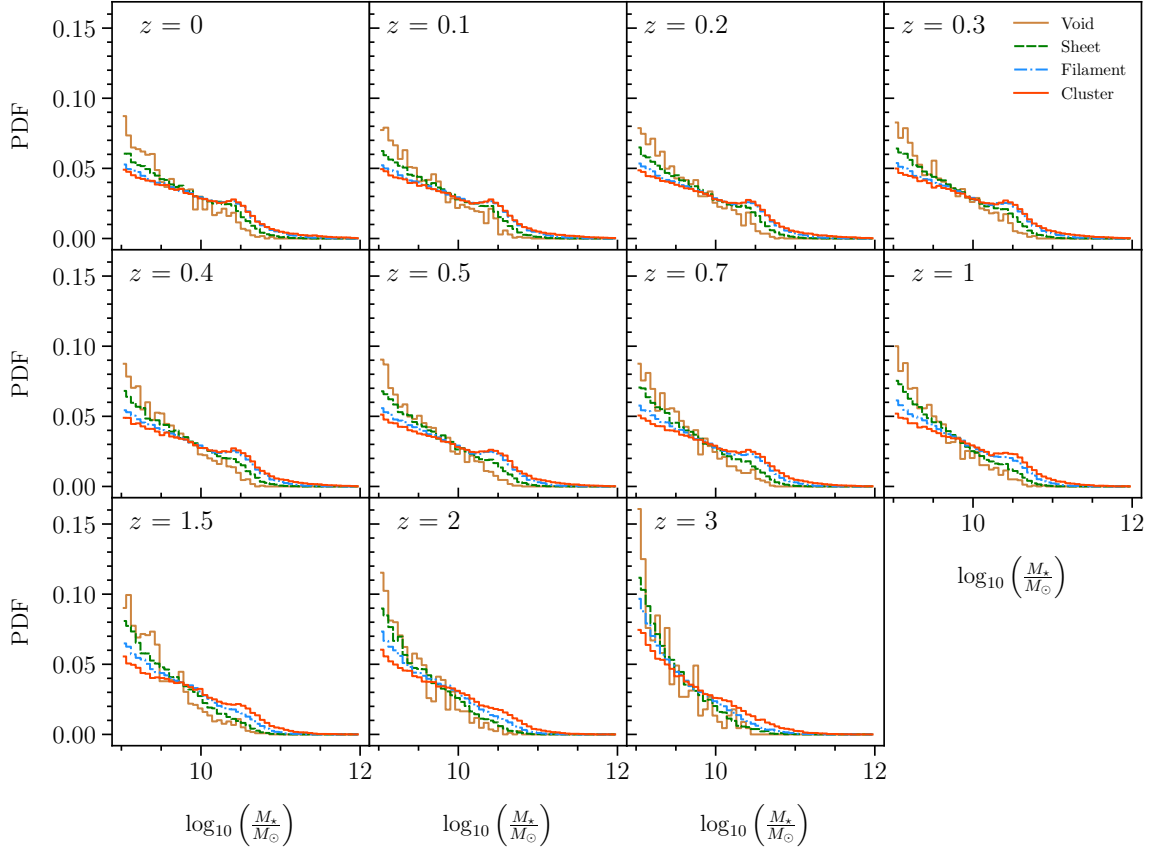
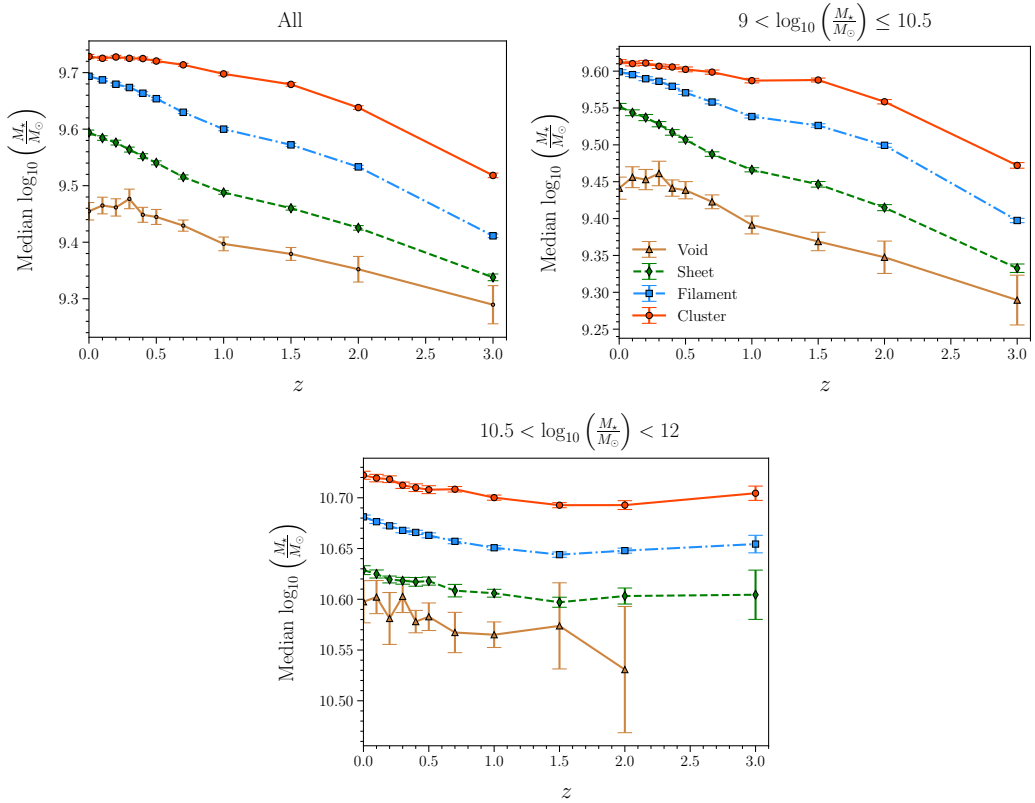**Figure 12**: Same as Figure 10 but for stellar mass.

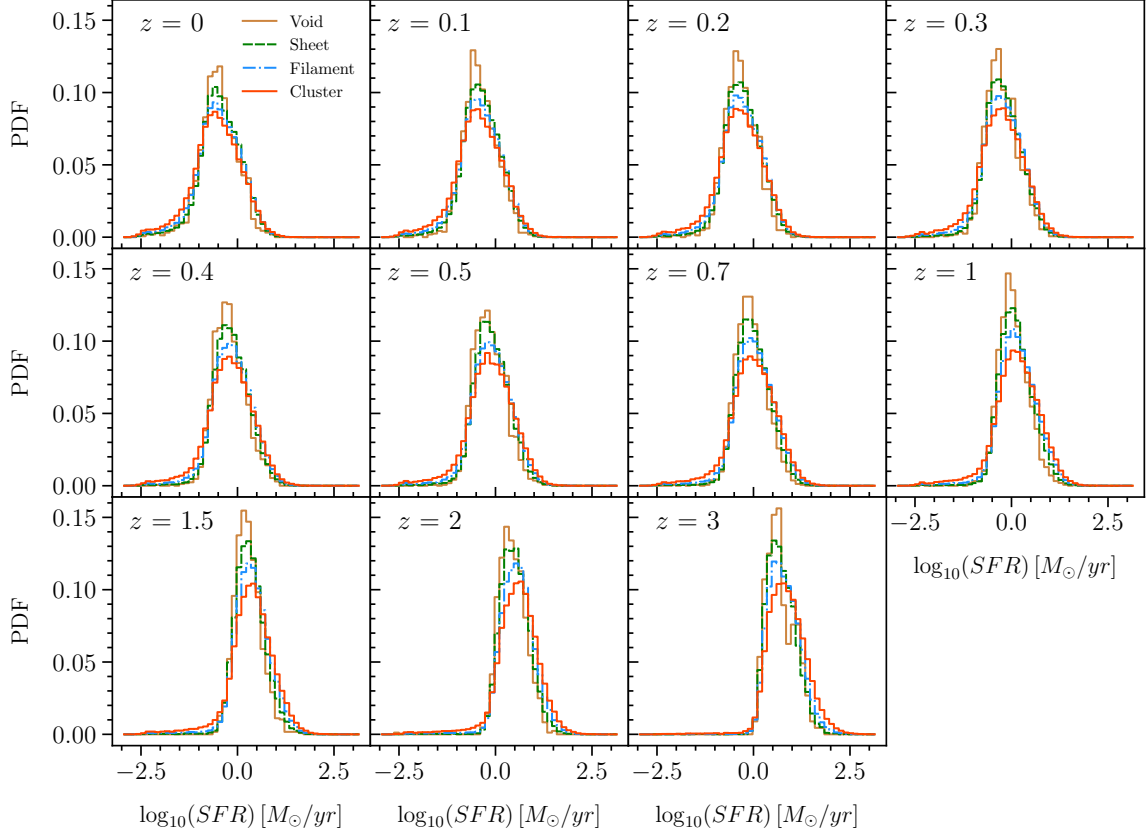**Figure 13**: Same as Figure 11 but for stellar mass.

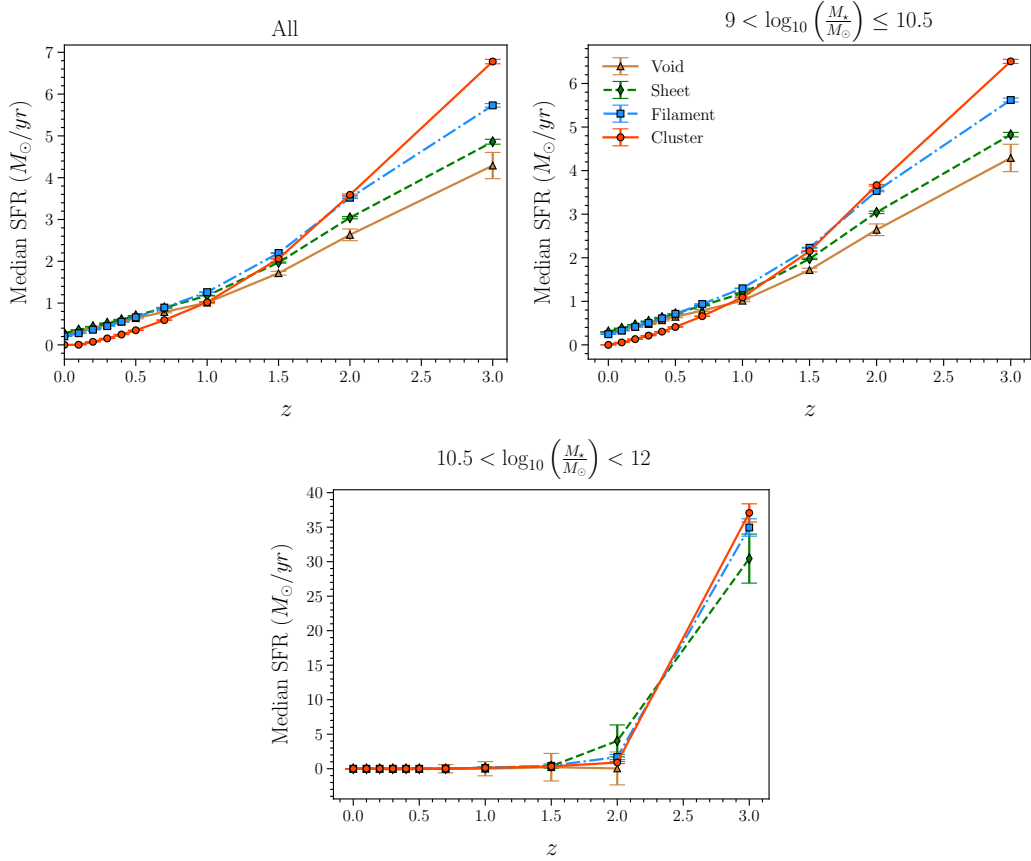**Figure 14**: Same as Figure 10 but for SFR.

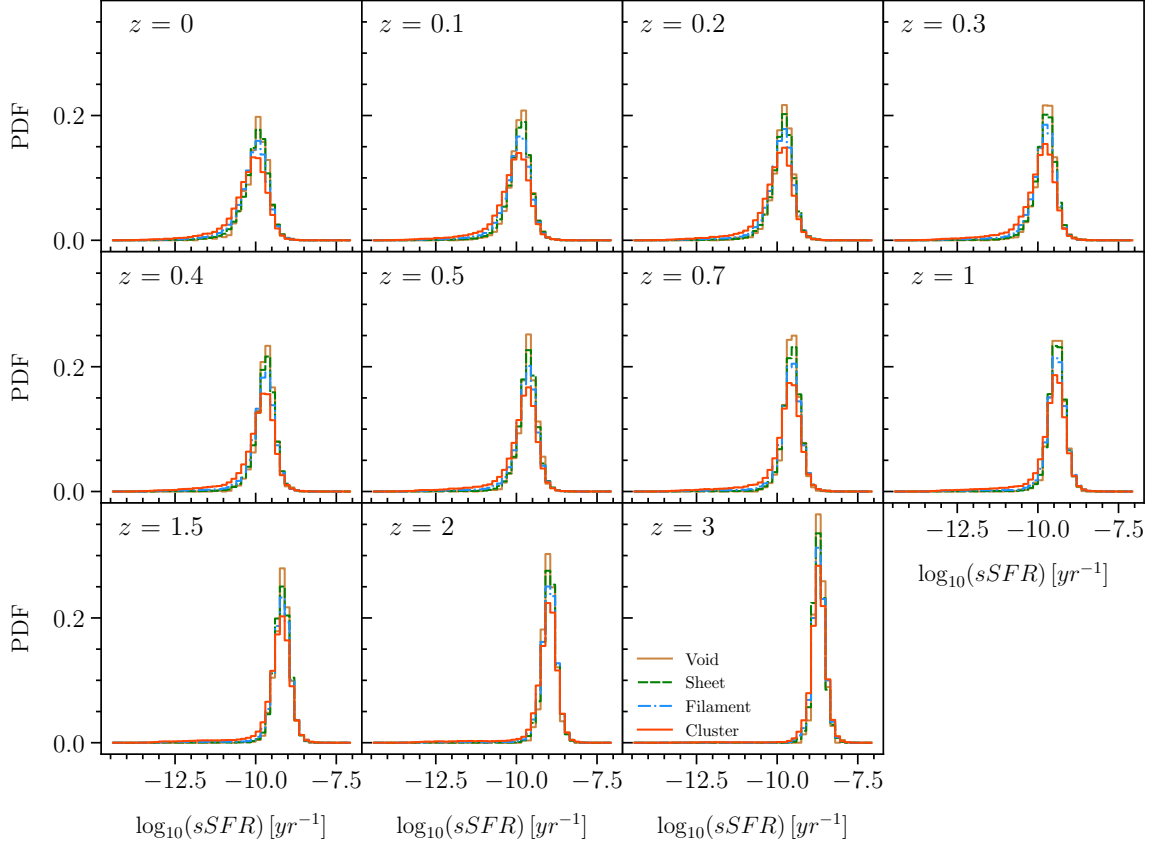**Figure 15**: Same as Figure 11 but for SFR.
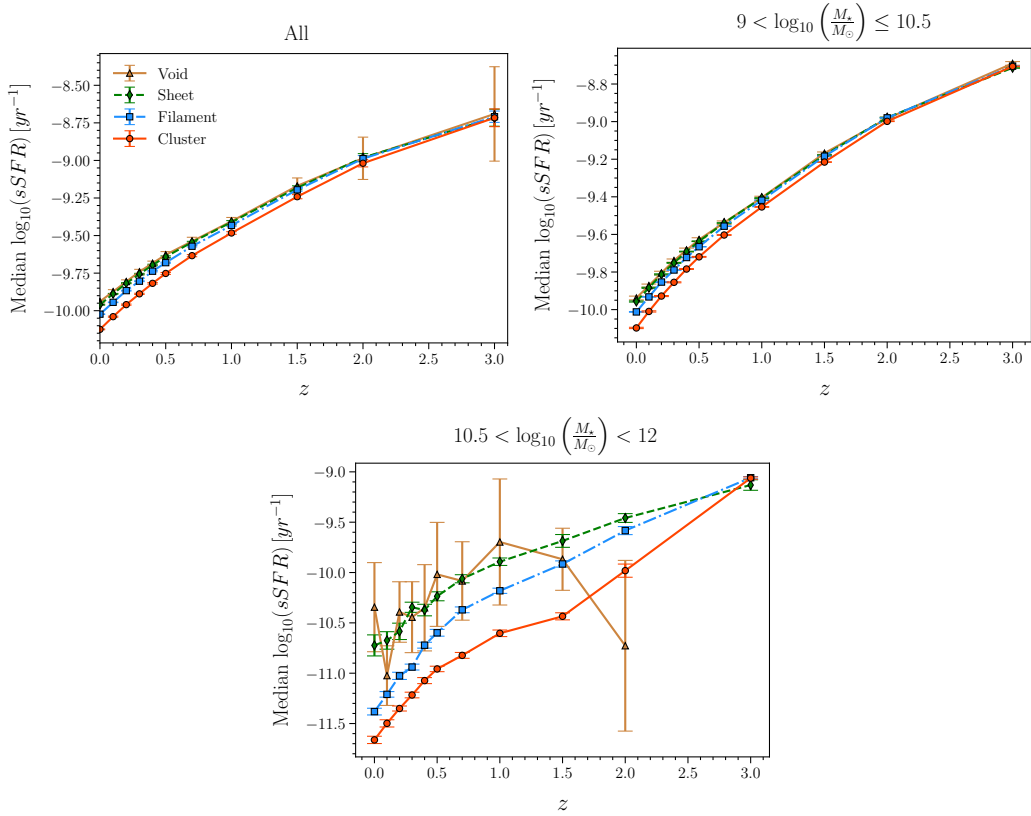
Figure 16: Same as Figure 10 but for sSFR.

Figure 17: Same as Figure 11 but for sSFR.

environments at $z < 1$. The results for the lower mass bin, shown in the top right panel of Figure 15, exhibit a similar trend to that observed in the entire sample. The bottom panel of Figure 15 indicates that the median SFR for massive galaxies ($\log(\frac{M_*}{M_\odot}) > 10.5$) drops to zero at $z \sim 1.5$ across all environments, suggesting that star formation in high-mass galaxies is strongly suppressed in the low-redshift universe.

4.8 Evolution of sSFR across diverse cosmic web environments

We show the distribution of specific star formation rate (sSFR) across cosmic web environments at various redshifts in the panels of Figure 16. While the star formation rate (SFR) measures the degree of star formation in a galaxy, sSFR normalizes this rate by its stellar mass. This normalization is crucial for comparing star formation activity across galaxies of different sizes, offering insights into the efficiency of star formation relative to galaxy mass. The panels in Figure 16 reveal trends similar to those seen in Figure 14. Specifically, the peak of the sSFR distribution in each environment shifts towards more negative values as redshift decreases. This gradual shift points to both internal and external mechanisms leading to the aging and transformation of galaxies in each type of environment. The peak amplitude is highest in voids, followed by sheets, filaments, and clusters. This indicates that, for a given stellar mass, star formation is strongest in less dense environments and becomes progressively weaker as the environment grows denser.

The median sSFR across different environments is shown in Figure 17. The top left panel indicates that, unlike the median SFR, there are no statistically significant differences in the median sSFR across environments in the redshift range $1.5 < z < 3$. As redshift decreases, sSFR decreases in all environments. At $z < 1$, clusters exhibit the lowest median sSFR, with filaments showing somewhat higher sSFR compared to clusters between $z = 1$ and $z = 0$. Sheets and voids have the highest and similar median sSFR in this redshift range. The top right panel presents results for the lower mass bin, which mirrors the trends observed in the entire sample for the reasons discussed earlier. The bottom panel of Figure 17 displays results for the higher mass bin. This panel shows similar trends but with larger differences in median sSFR across environments. It is interesting to note that the median sSFR for massive galaxies in voids tends to increase between $z = 2$ and $z = 1$, though this trend is difficult to confirm due to large errorbars for the galaxies in voids.

5 Discussions and Conclusions

We study the evolution of red and blue galaxies in different cosmic web environments using IllustrisTNG simulation. Our key findings are summarized as follows.

(i) We track the evolution of the red and blue fractions across different cosmic web environments from redshift $z = 3$ to $z = 0$. Initially, blue galaxies are more prevalent in clusters compared to other geometric environments. This trend reverses at lower redshifts. The red fraction starts to rise after specific redshifts for each environment, with clusters experiencing earlier suppression of star formation compared to filaments, sheets, and voids. The massive galaxies show a consistent increase in red fractions over time in all environments.

(ii) We analyze the red and blue fractions as a function of stellar mass across different environments at various redshifts. At $z = 3$, clusters have a higher blue fraction and lower red fraction compared to other environments at all masses, with filaments showing an intermediate blue fraction. Over time, the red fraction increases in higher mass galaxies and decreases in lower mass galaxies at all environments until $z = 1.5$. A pronounced environment-dependent trend emerges at $z < 1$ during which all environments show a significant increase in the red fraction at higher masses. On the other hand, clusters show a significant rise whereas other environments display a moderate increase in the red fraction at lower masses. The quenching in lower mass galaxies is more influenced by their geometric environment compared to the higher mass galaxies.

(iii) We study the relative fractions of red and blue galaxies across different cosmic web environments. Filaments and sheets show a decrease in the relative red fraction (RRF) and an increase in the relative blue fraction (RBF) with decreasing redshift, while clusters exhibit the opposite trend. For lower mass galaxies, the trends in RRF and RBF are consistent with the entire sample. For higher

mass galaxies, clusters initially have higher RRF and RBF than filaments. This trend reverses around $z \sim 1$. The differences in RRF and RBF across different geometric environments are primarily decided by the varying proportions of galaxies in these environments.

(iv) We investigate how the RRF and RBF of galaxies change with stellar mass and redshift in various cosmic web environments. Initially, the RRF is higher for lower mass galaxies in filaments compared to those in clusters. However, as redshift decreases, the RRF in clusters gradually surpasses that in filaments. The RRF in clusters at lower masses increases with decreasing redshift, making clusters dominant for low-mass red galaxies and filaments for intermediate masses. The RRF for clusters dominates at higher masses at all redshifts. It does not change significantly across the redshift range $3-0$, implying that massive ($\log(\frac{M_*}{M_\odot}) > 11$) red galaxies are mostly found in galaxy clusters. At lower masses, the RRF in clusters remains between $\sim (30-40)\%$ in this redshift range. On the other hand, RBF in filaments consistently have a higher relative proportion ($\sim (50-60)\%$) of blue galaxies, particularly at lower masses. This suggests that they host a diverse galaxy population, most likely due to less intense environmental quenching. The clusters, despite being densest, exhibit highest RBF at higher masses, indicating potential rejuvenation of star formation through interactions or mergers.

(v) The $(u-r)$ colour distribution of galaxies is unimodal at higher redshift and gradually shifts towards redder values over time, eventually showing bimodality by $z = 2$, with the red peak growing most in clusters. At $z < 1$, clusters have the highest median colour followed by filaments, sheets, and voids. The median colours of massive galaxies do not differ significantly across various environments in this redshift range implying that colour evolution is largely driven by mass rather than environment.

(vi) Clusters exhibit highest median mass followed by filaments, sheets and voids at all redshifts. The median stellar mass of galaxies increases with decreasing redshift across all environments. We observe a slower growth of median mass for lower mass galaxies in clusters at $z < 1$. In contrast, the median mass for higher mass galaxies remain stable during $z = 3 - 1.5$ and gradually increases at $z < 1$ in all environments. The median SFR declines with decreasing redshift in all environments, with clusters dominating until $z = 1.5$. At $z < 1.5$, the median SFR in clusters levels out across environments and then decreases relative to others. Notably, the median SFR for massive galaxies drops to zero in all environments at $z < 1.5$, indicating suppression of star formation in high-mass galaxies. The median sSFR decreases in all environments with decreasing redshifts with no significant differences across environments until $z = 1.5$. At $z < 1.5$, clusters exhibit the lowest median sSFR and voids and sheets exhibiting the highest values. The higher mass galaxies show larger variations in sSFR across environments.

Our study suggests that both stellar mass and geometric environments play an important role in galaxy evolution. The higher density regions host a larger fraction of blue galaxies during $z = 3 - 2$, implying they provide a more favourable environment for star formation. However, the environmental factors start to dominate at $z < 2$ reversing this trend. We find that at $z < 1$, most of the massive galaxies ($\log(\frac{M_*}{M_\odot}) > 10.5$) are quenched irrespective of their geometric environments. This is consistent with AGN feedback model in the IllustrisTNG simulations which suggests that AGN feedback is highly effective in massive central galaxies ($\log(\frac{M_*}{M_\odot}) > 10.5$) [128]. Kinetic feedback from super-massive black holes (SMBHs) is the key mechanism driving the quenching of star formation in massive galaxies [129]. The fraction of quenched galaxies in TNG300 is in the range $(30-80)\%$ percent in the stellar mass range $10^{10.5}-10^{11.5} M_\odot$ [127]. Our results (Figure 3, Figure 4) are consistent with these findings. So the AGN feedback may have played a dominant role in quenching the high mass galaxies in all environments. However, the AGN feedback model in IllustrisTNG shows reduced effectiveness in quenching galaxies of intermediate and lower masses [128]. At lower masses ($\log(\frac{M_*}{M_\odot}) < 10.5$), quenching is largely controlled by environment. The fraction of red galaxies at lower masses increases with decreasing redshift at each geometric environment. At lower masses, clusters host the highest fraction of red galaxies followed by filaments, sheets and voids. Low mass galaxies often undergo environmental quenching before they become part of their current host group. The pre-processing can involve interactions with other galaxies or the effects of the surrounding medium, leading to a reduction in their gas reservoirs and star formation rates.

The relative fractions of red and blue galaxies (RRF and RBF) are influenced by both stellar mass and geometric environment. Generally, RRF increases and RBF decreases in clusters as redshift

decreases. In contrast, filaments and sheets exhibit the opposite trend. At higher masses, both RRF and RBF in clusters decline with decreasing redshift, while in filaments, both show a steady increase. This anomalous behavior can be largely attributed to a growing relative abundance of intermediate and high-mass galaxies in filaments. Interestingly, clusters, despite being the densest environments, display the highest RRF and RBF for galaxies with masses $\log(\frac{M_*}{M_\odot}) > 11$. This suggests that massive galaxies are predominantly located in clusters, where most are quenched, although some may be rejuvenated through interactions or mergers. In contrast, filaments host a more diverse galaxy population as evidenced by the higher RBF and RRF at lower masses ($\log(\frac{M_*}{M_\odot} < 11)$. At lower masses, filaments exhibit relative red fractions (RRF) comparable to clusters, yet host nearly 60% of blue galaxies. This suggests that the milder environmental quenching in filaments enables galaxies to undergo a wider range of evolutionary stages. A recent study [90] using the SIMBA simulation [91] suggest that shock heating in filaments can inhibit star formation. Another study [92] with the IllustrisTNG simulation finds that satellite galaxies are especially susceptible to such quenching. Our results are consistent with these findings. The low-mass quenched galaxies in filaments may represent satellite populations, while the star-forming galaxies may correspond to central galaxies with intermediate masses.

Our study reveals several key trends in galaxy evolution across different geometric environments over time. At higher redshifts, the $(u - r)$ colour distribution is unimodal but turns into bimodal by $z = 2$, particularly in clusters, which have the highest median colour at $z < 1$. The median colour and stellar mass of galaxies increases steadily from $z = 3$ ato $z = 0$. For massive galaxies, a steady increase in median colour across all environments, with little variations across environments, suggests that the process driving the reddening of massive galaxies is fairly uniform across the cosmic web. This could indicate that the quenching mechanisms, such as AGN feedback, which cause galaxies to evolve from blue to red, operate similarly across different environments. In contrast, the significant differences in median stellar mass across environments suggest that the growth of galaxy mass is more sensitive to the local cosmic web environment, with different environments supporting different rates of stellar mass buildup. This might reflect environmental factors influencing galaxy mergers or accretion more strongly than colour evolution. This is further supported by the decline in SFR and sSFR across all environments, with massive galaxies showing a sharp reduction in these rates at lower redshifts, regardless of their environment.

We also compare our results with the earlier studies on galaxy evolution with hydrodynamical simulations. [109] investigate the evolution of galaxy colour using the EAGLE simulation [130] and find that the red sequence forms around $z \sim 1$ due to the quenching of low-mass satellite galaxies and AGN feedback in more massive central galaxies. [111] demonstrate using TNG100 and TNG300 that between 70% and 90% of central and satellite galaxies with masses greater than or equal to $\log(\frac{M_*}{M_\odot}) > 10$ are predicted to be quenched in the redshift range $0 \leq z \leq 0.5$. [110] demonstrate that in the EAGLE simulation, the quenching time scales for both central and satellite galaxies decrease with increasing stellar mass. They observe an increase in the fraction of passive galaxies at lower redshifts. Another study [112] using the TNG simulation finds that slow-quenching galaxies are approximately twice as common as fast-quenching galaxies in the redshift range of $0.7 < z < 2$. More recently, [113] study the roles of local density and interactions on the evolution of red and blue galaxies in the redshift range $0 \leq z \leq 3$ using the EAGLE simulation. They report that red galaxies tend to occupy denser regions and show significantly stronger clustering compared to blue galaxies at $z < 2$. They also find a substantial decrease in the blue fraction in paired galaxies at $z < 1$ suggesting significant roles of interactions in galaxy evolution. Our results are consistent with these findings. Further, Our findings also align with the observational studies [97–99, 131], reinforcing the effectiveness of hydrodynamical simulations as a valuable tool for investigating galaxy formation and evolution.

Our study indicates that quenching at higher masses is mainly driven by stellar mass, whereas quenching in intermediate- and low-mass galaxies is influenced by a complex interplay between stellar mass and environment. We conclude that both stellar mass and cosmic web environments play a significant role in shaping colour bimodality and driving overall galaxy evolution.

ACKNOWLEDGEMENTS

Data availability

The data for IllustrisTNG simulations are publicly available at https://www.tng-project.org/data/. The data produced in this work will be shared on reasonable request to the authors.

References

[1] I. Strateva, et al., AJ, **122**, 1861 (2001)

[2] M. R. Blanton, et al., ApJ, **594**, 186 (2003)

[3] E. F. Bell, D. H. McIntosh, N. Katz, M. D. Weinberg, ApJS, **149**, 289 (2003)

[4] M. L Balogh, I. K. Baldry, R. Nichol, C. Miller, R. Bower, K. Glazebrook, 2004, ApJL, **615**, L101 (2004)

[5] I. K. Baldry, K. Glazebrook, J. Brinkmann, Ž. Ivezić, R. H. Lupton, R. C. Nichol, A. S. Szalay, ApJ, **600**, 681 (2004)

[6] M. Martig, F. Bournaud, R. Teyssier, & A. Dekel, ApJ, **707**, 250 (2009)

[7] Y. Birnboim, & A. Dekel, MNRAS, **345**, 349 (2003)

[8] A. Dekel, & Y. Birnboim, MNRAS, **368**, 2 (2006)

[9] D. Kereš , N. Katz, D. H. Weinberg, & R. Davé , MNRAS, **363**, 2 (2005)

[10] J. M. Gabor, R. Davé , K. Finlator, & B. D. Oppenheimer, MNRAS, **407**, 749 (2010)

[11] Y.-. jie Peng ., A. Renzini, MNRAS, **491**, L51 (2020)

[12] K. L. Masters, M. Mosleh, A. K. Romer, R. C. Nichol, S. P. Bamford, K. Schawinski, C. J. Lintott, et al., MNRAS, **405**, 783 (2010)

[13] J. E. Gunn, & J. R. Gott, ApJ, **176**, 1 (1972)

[14] T. J. Cox, J. Primack, P. Jonsson, & R. S. Somerville, ApJL, **607**, L87 (2004)

[15] N. Murray, E. Quataert, & T. A. Thompson, ApJ, **618**, 569 (2005)

[16] V. Springel, T. Di Matteo, & L. Hernquist, MNRAS, **361**, 776 (2005)

[17] D. W. Hogg, et al., ApJ Letters, **601**, L29 (2004)

[18] I. K. Baldry, M. L. Balogh, R. Bower, K. Glazebrook, R. C. Nichol, AIP Conference Proceedings, **743**, 106 (2004)

[19] M. R. Blanton, D. Eisenstein, D. W. Hogg, D. J. Schlegel, J. Brinkmann, ApJ, **629**, 143 (2005)

[20] C. Park, et al. 2005, ApJ, **633**, 11 (2005)

[21] B. Pandey, & S. Bharadwaj, MNRAS, **357**, 1068 (2005)

[22] B. Pandey & S. Bharadwaj, MNRAS, **377**, L15 (2007)

[23] I. Zehavi, et al., ApJ, **630**, 1 (2005)

[24] B. Pandey, & S. Bharadwaj, MNRAS, **372**, 827 (2006)

[25] N. M. Ball, J. Loveday, R. J. Brunner, MNRAS, **383**, 907 (2008)

[26] S. P. Bamford, R. C. Nichol, I. K. Baldry, et al., MNRAS, **393**, 1324 (2009)

[27] M. C. Cooper, A. Gallazzi, J. A. Newman, R. Yan, MNRAS, **402**, 1942 (2010)

[28] B. Pandey, S. Sarkar, MNRAS, **498**, 6069 (2020)

[29] A. Nandi, B. Pandey, P. Sarkar, JCAP, **2024**, 012 (2024)

[30] P. F. Hopkins, L. Hernquist, T. J. Cox, D. Kereš, ApJS, **175**, 356 (2008)

[31] B. Moore, N. Katz, G. Lake, A. Dressler, & A. Oemler, A., Nature, **379**, 613 (1996)

[32] B. Moore, G. Lake, & N. Katz, N., ApJ, **495**, 139 (1998)

[33] M. L. Balogh, J. F. Navarro, & S. L. Morris, ApJ, **540**, 113 (2000)

[34] R. B. Larson, B. M. Tinsley, & C. N. Caldwell, ApJ, **237**, 692 (1980)

[35] R. S. Somerville, & J. R. Primack, MNRAS, **310**, 1087 (1999)

[36] D. Kawata, & J. S. Mulchaey, ApJL, **672**, L103 (2008)

[37] M. Geha, M. R. Blanton, R. Yan, J. L. Tinker, ApJ, **757**, 85 (2012)

[38] A. Toomre, J. Toomre, ApJ, **178**, 623 (1972)

[39] J. E. Barnes, L. Hernquist, ApJ, **471**, 115 (1996)

[40] J. C. Mihos, L. Hernquist, ApJ, **464**, 641 (1996)

[41] P. B. Tissera, R. Domínguez-Tenreiro, C., Sáiz A. Scannapieco, MNRAS, **333**, 327 (2002)

[42] T. J. Cox, P. Jonsson, J. R. Primack, R. S. Somerville, MNRAS, **373**, 1013 (2006)

[43] M. Montuori, P. Di Matteo, M. D. Lehnert, F. Combes, B. Semelin, A&A, **518**, A56 (2010)

[44] J. M. Lotz, P. Jonsson, T. J. Cox, D. Croton, J. R. Primack, R. S. Somerville, K. Stewart, ApJ, **742**, 103 (2011)

[45] P. Torrey, T. J. Cox, L. Kewley, L. Hernquist, ApJ, **746**, 108 (2012)

[46] P. F. Hopkins, T. J. Cox, L. Hernquist, D. Narayanan, C. C. Hayward, N. Murray, MNRAS, **430**, 1901 (2013)

[47] F. Renaud, F. Bournaud, K. Kraljic, P.-A. Duc, MNRAS, **442**, L33 (2014)

[48] F. Renaud, F. Bournaud, P.-A. Duc, MNRAS, **446**, 2038 (2015)

[49] J. Moreno, P. Torrey, S. L. Ellison, D. R. Patton, A. F. L. Bluck, G. Bansal, L. Hernquist, MNRAS, **448**, 1107 (2015)

[50] J. Moreno, P. Torrey, S. L. Ellison, D. R. Patton, C. Bottrell, A. F. L. Bluck, M. H. Hani, et al., MNRAS, **503**, 3113 (2021)

[51] F. Renaud, O. Segovia Otero, O. Agertz, MNRAS, **516**, 4922 (2022)

[52] A. Das, B. Pandey, S. Sarkar, RAA, **23**, 115018 (2023)

[53] R. B. Larson, B. M. Tinsley, ApJ, **219**, 46 (1978)

[54] E. J. Barton, M. J. Geller, S. J. Kenyon, ApJ, **530**, 660 (2000)

[55] D. G. Lambas, P. B. Tissera, M. S. Alonso, G. Coldwell, MNRAS, **346**, 1189 (2008)

[56] M. S. Alonso, P. B. Tissera, G. Coldwell, D. G. Lambas, MNRAS, **352**, 1081 (2004)

[57] B. Nikolic, H. Cullen, P. Alexander, MNRAS, **355**, 874 (2004)

[58] D. F. Woods, M. J. Geller, E. J. Barton, AJ, **132**, 197 (2006)

[59] D. F. Woods, M. J. Geller, AJ, **134**, 527 (2007)

[60] E. J. Barton, J. A. Arnold, A. R. Zentner, J. S. Bullock, R. H. Wechsler, ApJ, **671**, 1538 (2007)

[61] S. L. Ellison, D. R. Patton, L. Simard, A. W. McConnachie, AJ, **135**, 1877 (2008)

[62] S. L. Ellison, D. R. Patton, L. Simard, A. W. McConnachie, I. K. Baldry, J. T. Mendel, MNRAS, **407**, 1514 (2010)

[63] D. F. Woods, M. J. Geller, M. J. Kurtz, E. Westra, D. G. Fabricant, I. Dell'Antonio, AJ, **139**, 1857 (2010)

[64] D. R. Patton, S. L. Ellison, L. Simard, A. W. McConnachie, J. T. Mendel, MNRAS, **412**, 591 (2011)

[65] J. K. Barrera-Ballesteros, S. F. Sánchez, B. García-Lorenzo, J. Falcón-Barroso, D. Mast, R. García-Benito R., B. Husemann, et al., A&A, **579**, A45 (2015)

[66] M. D. Thorp, S. L. Ellison, H.-A. Pan, L. Lin, D. R. Patton, A. F. L. Bluck, D. Walters, et al., MNRAS, **516**, 1462 (2022)

[67] E. A. Shah, J. S. Kartaltepe, C. T. Magagnoli, I. G. Cox, C. T. Wetherell, B. N. Vanderhoof, K. C. Cooke, et al., ApJ, **940**, 4 (2022)

[68] A. Das, B. Pandey, S. Sarkar S., RAA, **23**, 025016 (2022)

[69] S. A. Gregory, L. A. Thompson, ApJ, **222**, 784 (1978)

[70] M. Joeveer, J. Einasto, IAUS, **79**, 241 (1978)

[71] J. Einasto, M. Joeveer, E. Saar, MNRAS, **193**, 353 (1980)

[72] I. B. Zeldovich, S. F. Shandarin, PAZh, **8**, 131 (1982)

[73] J. Einasto, A. A. Klypin, E. Saar, S. F. Shandarin, MNRAS, **206**, 529 (1984)

[74] J. R. Bond, L. Kofman, & D. Pogosyan, Nature, **380**, 603 (1996)

[75] S. Bharadwaj, V. Sahni, B. S. Sathyaprakash, S. F. Shandarin, C. Yess, ApJ, **528**, 21 (2000)

[76] M. A. Aragón-Calvo, R. van de Weygaert, B. J. T. Jones, MNRAS, **408**, 2163 (2010)

[77] N. I. Libeskind, R. van de Weygaert, M. Cautun, B. Falck, E. Tempel, T. Abel, M. Alpaslan, et al., MNRAS, **473**, 1195 (2018)

[78] M. A. Aragón-Calvo, E. Platen, R. van de Weygaert, A. S. Szalay, ApJ, **723**, 364 (2010)

[79] M. Cautun, R. van de Weygaert, B. J. T. Jones, C. S. Frenk, 2014, MNRAS, **441**, 2923 (2014)

[80] N. S. Ramachandra, S. F. Shandarin, MNRAS, **452**, 1643 (2015)

[81] W. Wang, P. Wang, H. Guo, X. Kang, N. I. Libeskind, D. Galárraga-Espinosa, V. Springel, et al., MNRAS, in press, (2024)

[82] S. Bharadwaj, S. P. Bhavsar, J. V. Sheth, ApJ, **606**, 25 (2004)

[83] B. Pandey, G. Kulkarni, S. Bharadwaj, T. Souradeep, MNRAS, **411**, 332 (2011)

[84] P. Sarkar, B. Pandey, S. Sarkar, MNRAS, **519**, 3227 (2023)

[85] T. Tuominen, J. Nevalainen, E. Tempel, T. Kuutma, N. Wijers, J. Schaye, P. Heinämäki, et al., A&A, **646**, A156 (2021)

[86] D. Galarraga-Espinosa, N. Aghanim, M. Langer, H. Tanimura, A&A, **649**, A117 (2021)

[87] Y.-C. Chen, S. Ho, R. Mandelbaum, N. A. Bahcall, J. R. Brownstein, P. E. Freeman, C. R. Genovese, et al., MNRAS, **466**, 1880 (2017)

[88] A. Singh, S. Mahajan, J. S. Bagla, MNRAS, **497**, 2265 (2020)

[89] M. Hoosain, S.-L. Blyth, R. E. Skelton, S. J. Kannappan, D. V. Stark, K. D. Eckert, Z. L. Hutchens, et al., MNRAS, **528**, 4139 (2024)

[90] T.-E. Bulichi, R. Dav'e, K. Kraljic, MNRAS, **529**, 2595 (2024)

[91] R. Dav'e, D. Angl'es-Alc'azar, D. Narayanan, Q. Li, M. H. Rafieferantsoa, S. Appleby, MNRAS, **486**, 2827 (2019)

[92] F. Hasan, J. N. Burchett, D. Hellinger, O. Elek, D. Nagai, S. M. Faber, J. R. Primack, et al., ApjL, Accepted, arXiv:2311.01443 (2024)

[93] E. Roediger, M. Brüggen, MNRAS, **380**, 1399 (2007)

[94] R. Ruggiero, G. B. Lima Neto, MNRAS, **468**, 4107 (2017)

[95] M. Einasto, R. Kipper, P. Tenjes, J. Einasto, E. Tempel, L. J. Liivamägi, A&A, **668**, A69 (2022)

[96] A. M. Rodríguez-Medrano, V. Springel, F. A. Stasyszyn, D. J. Paz, MNRAS, **528**, 2822 (2024)

[97] K.-V. H. Tran, C. Papovich, A. Saintonge, M. Brodwin, J. S. Dunlop, D. Farrah, K. D. Finkelstein, et al., ApJL, **719**, L126 (2010)

[98] A. Gupta, K.-V. Tran, J. Cohn, L. Y. Alcorn, T. Yuan, V. Rodriguez-Gomez, A. Harshan, et al., 2020, ApJ, **893**, 23 (2020)

[99] P. Madau, H. C. Ferguson, M. E. Dickinson, M. Giavalisco, C. C. Steidel, & A. Fruchter, MNRAS, **283**, 1388 (1996)

[100] E. F. Bell, C. Wolf, K. Meisenheimer, H.-W. Rix, A. Borch, S. Dye, M. Kleinheinrich, et al., ApJ, **608**, 752 (2004)

[101] S. M. Faber, C. N. A. Willmer, C. Wolf, D. C. Koo, B. J. Weiner, J. A. Newman, M. Im, et al., ApJ, **665**, 265 (2007)

[102] D. Nelson, A. Pillepich, V. Springel, R. Weinberger, L. Hernquist, R. Pakmor, S. Genel, et al., MNRAS, **475**, 624 (2018)

[103] D. Nelson, V. Springel, A. Pillepich, V. Rodriguez-Gomez, P. Torrey, S. Genel, M. Vogelsberger, et al., 2019, Computational Astrophysics and Cosmology, **6**, 2 (2019)

[104] V. Springel, R. Pakmor, A. Pillepich, R. Weinberger, D. Nelson, L. Hernquist, M. Vogelsberger M., et al., MNRAS, **475**, 676 (2018)

[105] A. Pillepich, V. Springel, D. Nelson, S. Genel, J. Naiman, R. Pakmor, L. Hernquist, et al., MNRAS, **473**, 4077 (2018)

[106] F. Marinacci, M. Vogelsberger, R. Pakmor, P. Torrey, V. Springel, L. Hernquist, D. Nelson, et al., MNRAS, **480**, 5113 (2018)

[107] J. P. Naiman, A. Pillepich, V. Springel, E. Ramirez-Ruiz, P. Torrey, M. Vogelsberger, R. Pakmor, et al., MNRAS, **477**, 1206 (2018)

[108] M. Furlong, R. G. Bower, T. Theuns, J. Schaye, R. A. Crain, M. Schaller, C. Dalla Vecchia, et al., MNRAS, **450**, 4486 (2015)

[109] J. W. Trayford, T. Theuns, R. G. Bower, R. A. Crain, C. del P. Lagos, M. Schaller, J. Schaye, MNRAS, **460**, 3925 (2016)

[110] R. J. Wright, C. del P. Lagos, L. J. M. Davies, C. Power, J. W. Trayford, O. I. Wong, MNRAS, **487**, 3740 (2019)

[111] M. Donnari, A. Pillepich, G. D. Joshi, D. Nelson, S. Genel, F. Marinacci, V. Rodriguez-Gomez, et al., MNRAS, **500**, 4004 (2021)

[112] D. Walters, J. Woo, S. L. Ellison, MNRAS, **511**, 6126 (2022)

[113] A. Das, B. Pandey, JCAP, **08**, 060 (2024)

[114] B. Pandey, Astronomy and Computing, **44**, 100725 (2023)

[115] N. Otsu, IEEE Transactions on Systems, Man, and Cybernetics, **9**, 62 (1979)

[116] V. Springel, 2010, MNRAS, **401**, 791 (2010)

[117] R. Weinberger, V. Springel, R. Pakmor, ApJS, **248**, 32 (2020)

[118] M. Vogelsberger, S. Genel, D. Sijacki, P. Torrey, V. Springel, L. Hernquist, MNRAS, **436**, 3031 (2013)

[119] M. Vogelsberger, S. Genel, V. Springel, P. Torrey, D. Sijacki, D. Xu, G. Snyder, et al., Nature, **509**, 177 (2014)

[120] S. Genel, M. Vogelsberger, V. Springel, D. Sijacki, D. Nelson, G. Snyder, V. Rodriguez-Gomez, et al., MNRAS, **445**, 175 (2014)

[121] Planck Collaboration, P. A. R. Ade, N. Aghanim, M. Arnaud, M. Ashdown, J. Aumont, C. Baccigalupi, et al., A&A, **594**, A13 (2016)

[122] V. Springel, S. D. M. White, G. Tormen, G. Kauffmann, MNRAS, **328**, 726 (2001)

[123] K. Dolag, S. Borgani, G. Murante, V. Springel, MNRAS, **399**, 497 (2009)

[124] V. Springel, L. Hernquist, MNRAS, **339**, 289 (2003)

[125] O. Hahn, C. Porciani, C. M. Carollo & A. Dekel, MNRAS, **381**, 41 (2007)

[126] J. E. Forero–Romero, Y. Hoffman, S. Gottlöber, A. Klypin, G. Yepes, MNRAS, **396**, 1815 (2009)

[127] M. Donnari, A. Pillepich, D. Nelson, M. Vogelsberger, S. Genel, R. Weinberger, F. Marinacci, et al., MNRAS, **485**, 4817 (2019)

[128] M. Donnari, A. Pillepich, G. D. Joshi, D. Nelson, S. Genel, F. Marinacci, V. Rodriguez-Gomez, et al., MNRAS, **500**, 4004 (2021)

[129] R. Weinberger, V. Springel, R. Pakmor, D. Nelson, S. Genel, A. Pillepich, M. Vogelsberger, et al., MNRAS, **479**, 4056 (2018)

[130] Schaye J. et al. (The EAGLE project), MNRAS, **446**, 521 (2015)

[131] N. M. Förster Schreiber, S. Wuyts, ARA&A, **58**, 661 (2020)